GEOCHEMISTRY OF THE GALÁPAGOS TRANSFORM FAULT

A Thesis

Presented in Partial Fulfillment of the Requirements for the

Degree of Master of Science

with a

Major in Geology

in the

College of Graduate Studies

University of Idaho

by

Thomas A. Morrow

August 2014

Major Professor: Karen S. Harpp, Ph.D.

Authorization to Submit

This thesis of Thomas Morrow, submitted for the degree of Master of Science with a Major in Geology and titled "Geochemistry of the Galápagos Transform Fault," has been reviewed in final form. Permission, as indicated by the signatures and dates below, is now granted to submit final copies to the College of Graduate Studies for approval.

Major Professor:	_____ Karen Harpp, Ph.D.	Date: _____
Committee Members:	_____ Eric L. Mittelstaedt, Ph.D.	Date: _____
	_____ Brian Kennedy, Ph.D.	Date: _____
Department Administrator:	_____ Mickey Gunter, Ph.D.	Date: _____
Discipline's College Dean:	_____ Paul Joyce, Ph.D.	Date: _____

Final Approval and Acceptance

Dean of the College of Graduate Studies:	_____ Jie Chen, Ph.D.	Date: _____

Abstract

The Galápagos plume has profoundly affected the development and evolution of the nearby (<250 km) Galápagos Transform Fault (GTF). We present major element, trace element, and radiogenic isotope analyses of samples collected from the GTF during SON0158, EWI0004, and MV1007 cruises. We find that GTF lavas are chemically distinct from nearby axial ridge lavas and off-axis seamounts. The GTF lavas are anomalously depleted in incompatible trace elements (ITEs) and have lower ratios of more incompatible to less incompatible trace elements relative to axial lavas; comparable ITE compositions are only observed >300 km from the plume center. We present a melting model that reproduces GTF lava chemistry from a mixture of melts from a two-component mantle. Model results predict that GTF lavas are produced by a mixture of ~4-5% partial melts of a mantle source that has previously undergone partial melting and is being re-melted beneath the TF.

Acknowledgements

I would like to thank the crew of the R/V *Melville* and the scientific party of the MV1007 FLAMINGO cruise, led by Dr. Karen Harpp. This project would not have been possible without their work and Dr. Harpp's expert guidance and knowledge. I would also like to thank committee members Dr. Eric Mittelstaedt and Dr. Brian Kennedy for their outstanding support and guidance in pursuit of my Master's degree. I am grateful for the opportunity provided to me by Dr. Tom Williams to come work at the University of Idaho as part of a skilled and fun department. I owe many thanks to fellow graduate students in my department for their support and advice, in particular, Emily W., Darin, Emma, James, Matt, Alex, Brady, and Emily M. A special thanks goes to my coach, office mate, mentor, and friend, Erika. I thank Dr. Mike Perfit at the University of Florida for inspiring me to pursue my advanced degree after receiving my Bachelor's. I am grateful for my family's support throughout this endeavor and their enthusiasm for science, which has driven me since I was a child. Funding for this project was provided by the National Science Foundation.

Dedication

This document is dedicated to the memory of my grandfather, Walter Davis, and everything he has taught me.

“Whatever.”

Table of Contents

List of Tables

List of Figures

1 Introduction and Background

Oceanic Transform Faults (TFs) are part of the mid-ocean ridge (MOR) system and are fundamental to accommodating plate tectonic motions (e.g., *Wilson*, 1965; *Sykes*, 1967). They offset MORs by 10s to 100s of kilometers (e.g., *Fox and Gallo*, 1984; *Macdonald et al.*, 1988) and, in some cases, are host to volcanic activity (e.g., *Lonsdale*, 1989; *Fornari et al.*, 1989). Transforms are a first-order feature of the MOR system; understanding their effect on mantle processes, such as melting and flow mechanics, is critical to understanding shallow mantle compositions and dynamics.

The Galápagos Transform Fault (GTF) is located ~150 km northeast of the surface expression of the Galápagos plume, the Galápagos Archipelago. Its formation is proposed to result directly from interaction between the Galápagos plume and the Galápagos Spreading Center (GSC) (e.g., *Wilson and Hey*, 1995; *Small*, 1995; *Mittelstaedt et al.*, 2012). On either side of the TF, mid-ocean ridge basalts (MORBs) from the GSC have plume-influenced chemical compositions (e.g., *Schilling et al.*, 1982; *Verma and Schilling*, 1982; *Verma et al.*, 1983; *Schilling et al.*, 2003; *Christie et al.*, 2005; *Ingle et al.*, 2010) indicative of material communication between the Galápagos plume and the ridge. The Galápagos Transform is influenced by the nearby plume and the composition of volcanic products sampled within the transform may provide insight into the composition of the plume-influenced mantle beneath the GSC.

Lavas erupted in transform valleys are typically more depleted in incompatible trace elements, have lower ratios of more incompatible to less incompatible trace elements, and have different radiogenic isotope compositions when compared to lavas deposited on adjacent ridge axes. These observations indicate that melting conditions and possibly even mantle sources beneath TFs differ from those beneath MORs (e.g., *Hékinian et al.*, 1995; *Wendt et al.*, 1999; *Saal et al.*, 2004; *Nagle et al.*, 2007). Previous works (e.g., *Perfit et al.*, 1996; *Wendt et al.*, 1999) suggest that TF melts sample more depleted mantle material than MORB melts. Transform lavas can be used to interpret a larger range of mantle source compositions when incorporated with observations at MORs.

In this study, I present the major, trace element, and radiogenic isotope compositions of volcanic samples from within the GTF. From these new observations I interpret the composition of the mantle source material supplying melts to the TF and then compare this to mantle sources of GSC and Northern Galápagos Volcanic Province (NGVP) lavas. The TF melt sources complement

perspectives on melt sources in the NGVP and GSC by revealing more depleted mantle compositions that may not be clearly expressed in GSC MORB or NGVP lavas.

1.1 A mantle plume beneath the Galápagos Archipelago

The Galápagos Archipelago is a group of volcanic islands in the Pacific Ocean (Figure 1) interpreted as the surface expression of a mantle plume (e.g., *Morgan*, 1971; *Geist et al.*, 1988; *Graham et al.*, 1993). There are 21 emergent volcanoes, 13 of which show signs of activity during the Holocene (e.g., *White et al.*, 1993), along with numerous seamounts and submarine cones, where cones are defined as circular volcanic edifices <200 m in relief (e.g., *Smith et al.*, 1988). The wide distribution of Galápagos volcanism and absence of a focused linear hotspot track is partly attributed to its estimated weak buoyancy flux (~1 Mgs^{-1}; *Sleep*, 1990). The Galápagos plume is classified as a moderate plume compared to other Pacific plumes, which have buoyancy fluxes that range from 0.3 Mgs^{-1} to 8.7 Mgs^{-1} (*Sleep*, 1990; *Schilling*, 1991).

Seismic studies suggest that there is a mantle plume beneath the Galápagos Archipelago (e.g., *Hooft et al.*, 2003; *Villagomez et al.*, 2007; *Villagomez et al.*, 2014). Modeled shear-wave velocities underneath the Galápagos Archipelago are found to be low, indicating asthenosphere having an excess temperature of 30-150°C and up to ~0.5% partial melt; the warm, partially molten material spreads northward along the lower boundary of oceanic lithosphere toward the GSC and is interpreted as spreading plume material (Figure 2) (*Villagomez et al.*, 2007, *Villagomez et al.*, 2014). Analysis of teleseismic receiver functions reveals a thinned mantle transition zone under the archipelago, interpreted as localized, anomalously hot (130±60°C) upwelling from the deep mantle (>400 km) (*Hooft et al.*, 2003).

In addition to seismic evidence, several geochemical indicators support the hypothesis of a geochemically distinct mantle plume supplying lavas to the Galápagos Archipelago. For example, radiogenic isotope ratios and incompatible trace element compositions in Galápagos lavas are consistent with contribution from an enriched, primitive mantle source underlying the Galápagos Archipelago (e.g., *Morgan*, 1971; *Geist et al.*, 1988; *Graham et al.*, 1993; *White et al.*, 1993; *Kurz and Geist*, 1999; *Jackson et al.*, 2008). Furthermore, elevated $^{3}He/^{4}He$ (up to 27 R/Ra) in lavas gathered from the westernmost islands in the archipelago are indicative of a deep, primitive mantle source (e.g., *Graham et al.*, 1993; *Kurz and Geist*, 1999). The observed radiogenic isotope enrichments in Pb, Sr, and Nd, as well as enrichments in incompatible trace elements Ti, Ta, and Nb, (TITAN elements; *Jackson et al.*, 2008), are similar to compositions at other hotspots, which are each

believed to be associated with a deep, thermal upwelling that initiates at or near the core-mantle boundary (e.g., *Geist et al.*, 1988; *Graham et al.*, 1993; *White et al.*, 1993; *Kurz and Geist*, 1999; *Harpp and White*, 2001; *Jackson et al.*, 2008).

Within the archipelago, radiogenic isotope ratios and trace element compositions in lavas vary from plume-like values to compositions similar to those of MORBs. Lavas enriched in radiogenic isotope ratios define a 'horseshoe' shape around the periphery of the archipelago with a core of more depleted material in the center (*Geist et al.*, 1988; *White et al.*, 1993; *Blichert-Toft and White*, 2001; *Harpp and White*, 2001); hypotheses for the presence of the depleted core include entrainment of upper mantle material into the upwelling plume (*Geist et al.*, 1988; *White et al.*, 1993; *Blichert-Toft and White*, 2001; *Harpp and White*, 2001), reincorporation of thermally eroded lithospheric material (*McBirney*, 1993), and a depleted component within the Galápagos plume (*Ito et al.*, 1997; *Hoernle et al.*, 2000; *Ingle et al.*, 2010).

These complex geochemical variations are attributed to varying contributions from different mantle reservoirs supplying material to Galápagos melts (*Hoernle et al.*, 2000; *Harpp and White*, 2001) coupled to a range of partial melting depths within the upwelling plume (*Villagomez et al.*, 2014). *Harpp and White* (2001) use principal component analysis of radiogenic isotope ratios (Pb, Sr, Nd) in Galápagos lavas to define four mantle reservoirs that contribute material to Galápagos Archipelago melts: PLUME, WD, FLO, and DUM. They propose that the PLUME and FLO end-members are intrinsic to the Galápagos plume (*Harpp and White*, 2001) and that the PLUME signature is derived from primitive lower mantle material. The DUM component is attributed to either ambient upper mantle entrained into the plume (e.g., *Harpp and White*, 2001) or a depleted component within the plume (e.g. *Hoernle et al.*, 2000). The origin of the WD component (enriched relative to other Galápagos compositions in $^{207}Pb/^{204}Pb$ and $^{208}Pb/^{204}Pb$ for a given $^{206}Pb/^{204}Pb$) is unclear. *Ingle et al.* (2010) and *Gibson et al.* (2012) suggest that the PLUME, FLO, and WD isotopic end-members are distributed throughout the Galápagos plume as discrete, small-scale (~10-100 km) heterogeneities within a matrix of depleted mantle material (DUM). Whereas *Harpp and White* (2001) and *Hoernle et al.* (2000) argue that larger-scale spatial variability in the Galápagos plume stem is responsible for the horseshoe-shaped distribution of isotopic enrichments in the Galápagos Archipelago. In contrast, *Villagomez et al.* (2014) propose that it is the onset of hydrous melting at variable depths in the upwelling plume that controls the variability of isotope and trace element enrichment in Galápagos lavas.

1.2 Evidence for plume-ridge interaction in the Galápagos

The Cocos and Nazca plates (Figure 1) are separated by the plume-influenced GSC, ~150-250 km north of the Galápagos Archipelago. Near the center of the Galápagos Transform (~90.8°W, 1.5°N) the Cocos plate is moving at a rate of ~87.3 mm yr-1 at an azimuth of ~41.4° and the Nazca plate is moving ~55.3 mm yr-1 at ~80.1° relative to a no-net-rotation reference frame (NNR-MORVEL56; *Argus et al.*, 2011). Approximately 600 km east and west of the Galápagos Archipelago, the GSC shoals gradually toward the hotspot (Figure 2A). Axial depths decrease from ~2500 m at 94°W and 86°W to <1700 m at 91.4°W. Across the same distance, the ridge axis transitions from a slow-spreading axial valley morphology to a fast-spreading axial high morphology, despite the intermediate spreading rate of the GSC (Figures 2B, C, D, and E) (*Canales et al.*, 1997; *Canales et al.*, 2002; *Detrick et al.*, 2002; *Sinton et al.*, 2003; *Christie et al.*, 2005). The deviation from slow- to fast-spreading axial morphology is attributed to increased magma supply from the Galápagos plume (*Canales et al.*, 1997).

Spreading center lava chemistry and axial morphology is also perturbed by the influence of the nearby plume (e.g., *Ito and Lin*, 1995; *Wilson and Hey*, 1995; *Canales et al.*, 1997; *Canales et al.*, 2002; *Detrick et al.*, 2002; *Schilling et al.*, 2003; *Cushman et al.*, 2004; *Christie et al.*, 2005; *Kokfelt et al.*, 2005). Previous studies of the GSC document ~1000 km-long gradients of enrichment in radiogenic isotope ratios (Pb, Sr, Nd) and incompatible trace element (ITE) ratios (e.g., K/Ti, La/Yb) in lavas sampled along the spreading center, with a peak enrichment near ~92°W (Figure 3) (*Schilling et al.*, 1982; *Verma and Schilling*, 1982; *Verma et al.*, 1983; *Detrick et al.*, 2002; *Schilling et al.*, 2003; *Cushman et al.*, 2004; *Christie et al.*, 2005; *Kokfelt et al.*, 2005; *Ingle et al.*, 2010). Near-hot spot ITE enrichments may indicate low extents of hydrous melting of plume-derived material (*Asimow and Langmuir*, 2003; *Cushman et al.*, 2004). *Ingle et al.* (2010) suggest that an isotopically depleted mantle component contributes to GSC lavas west of ~92°W and is distinct from the depleted component expressed in the Galápagos Archipelago. This depleted ridge component (*Ingle et al.*, 2010) may represent additional compositional zoning within the plume beyond the four components identified by *Harpp and White* (2001) or compositional zoning within the upper mantle underlying the GSC. In both cases, *Ingle et al.* (2010) suggest that deep buoyancy-driven flow is responsible for geochemical variations along the GSC, consistent with influence from the nearby mantle plume. With increasing along-axis distance from ~92°W (where the plume stem is closest to the GSC axis), lavas become more MORB-like in isotope and ITE ratios (*Schilling et al.*, 1982; *Verma*

and Schilling, 1982; *Verma et al.*, 1983; *Schilling et al.*, 2003). The depletion in radiogenic isotope ratios and ITE ratios may reflect progressive dilution of Galápagos plume material by depleted upper mantle (*Schilling et al.*, 1982; *Verma and Schilling*, 1982; *Verma et al.*, 1983; *Schilling et al.*, 2003).

Geophysical observations of gravity anomalies and thickened crust along the GSC further support hypotheses of plume-ridge interaction (e.g., *Canales et al.*, 2002; *Mittelstaedt et al.*, 2014). Part of the gravity anomaly along the western GSC and ~350 m of swell along the ridge axis is attributed to thermal and compositional anomalies in the mantle (*Ito and Lin*, 1995; *Canales et al.*, 2002). Ridge-parallel seismic refraction profiles along the western GSC indicate that crustal thickness increases by about 2.3 km near the hotspot (*Canales et al.*, 2002). East of the Galápagos Transform Fault (GTF) at 90.8°W, gravity-derived crustal thickness is ~1 km greater than along the west GSC (*Mittelstaedt et al.*, 2014). Moreover, *Canales et al.* (2014) argue that beneath the GSC, close to the plume (~92°W), melt fractions are up to 7% higher than at locations further from the plume; in addition to thickened crust, partial melts may contribute to the observed gravity anomaly (e.g., *Canales et al.*, 2002).

Within the NGVP, between the active spreading axis of the GSC and the archipelago, physical manifestations of plume-ridge interaction are readily observed in the form of volcanic lineaments (*Morgan*, 1971; *Harpp and Geist*, 2002; *Mittelstaedt et al.*, 2005; *Mittelstaedt et al.*, 2012) and elongate seamounts (*Harpp et al.*, 2003; *Mittelstaedt et al.*, 2012). Intra-plate volcanism in the NGVP is attributed to the NE-SW component of plate spreading at a rate of ~8 km Ma^{-1}, the obliquity of the 90.8°W transform fault (Figure 2), and interaction of spreading plume material with the overlying lithosphere (*Harpp and Geist*, 2002; *Harpp et al.*, 2003; *Mittelstaedt et al.*, 2005; *Mittelstaedt et al.*, 2012). *Harpp and Geist* (2002) suggest that extensionally-driven decompression melting of the underlying mantle supplies magma to the off-axis volcanoes, which is partially supported by numerical models that simulate extension-driven melting in the NGVP (*Mittelstaedt et al.*, 2012).

Tectonic reconstructions based upon modeling of magnetic anomalies indicate that multiple southward ridge jumps occurred over the past 5 million years as the GSC migrated north (Figure 5) (*Hey*, 1977; *Wilson and Hey*, 1995; *Mittelstaedt et al.*, 2012). After a jump, the newly active spreading axis of the GSC propagates a new ridge axis closer to the plume which, in some cases, may extend the 90.8°W transform offset (e.g., *Wilson and Hey*, 1995; *Meschede and Barckhausen*, 2000; *Mittelstaedt et al.*, 2012). Recently identified ridge jumps close to the plume occurred at least ~4.5 Ma when a segment of the GSC jumped ~20 km southward (Figure 5; *Mittelstaedt et al.*, 2012). At

~3.5 Ma, a second jump initiated a new segment that propagated westward, sub-parallel to the GSC; propagation of this segment has since ceased, forming the 93.3°W overlapping spreading center (Figure 2). Between 2.5 and 3.5 Ma, a third ridge jump relocated a segment of the eastern GSC southward, toward the plume (Figure 5), leading to formation of the northern section of the GTF (Figure 4B). At ~1 Ma, a ~30 km southward jump of the eastern GSC, followed by westward propagation of the new segment, extended the GTF (Figure 5) to create its current southern half (Figure 4C).

1.3 The 90.8°W Galápagos Transform: A plume-influenced transform fault

The Galápagos Transform Fault (GTF) at 90.8°W (Figure 4) strikes ~175°, ~15° from perpendicular to the strike of the GSC (*Sinton et al.*, 2003). The GTF valley is ~100 km long and between ~15 km and ~25 km wide. North of 1.15°N, the GTF is dominated morphologically by a 1 km deep extensional basin, ~3500 mbsl at its deepest point (Figure 4B) (*Sinton et al.*, 2003; *Mittelstaedt et al.*, 2012). South of 1.15°N, the TF valley is broader (~25 km) and shallower (~2600 mbsl) than the northern basin (Figure 4).

In models of TF formation (e.g., *Angelier et al.*, 2004; *Angelier et al.*, 2008; *Gerya*, 2013), transforms originate as Riedel shear zones (e.g., *Riedel*, 1929), developing faults oblique to the direction of shear motion across the transform, and subsequently evolve to a mature TF with identifiable strike-slip fault traces. The southern section of the GTF is morphologically similar to *Angelier et al.'s* (2004) first stage end-member and *Gerya's* (2013) models of the early stages of a proto-transform. In the southern section of the GTF, faults are oblique to the spreading direction and the general strike of the GTF (*Mittelstaedt et al.*, 2012), similar to a Riedel distribution. The motion along these faults is not constrained, and we cannot determine whether the southern half of the transform exhibits Riedel's type R' or R distribution (equivalent to *Angelier et al.*'s (2004) first stage or second stage of transform development), though the strike of these faults and relative plate motion across the TF is consistent with the latter. The southern section of the GTF lacks a definitive fault trace that identifies *Angelier et al.*'s (2004) mature transform and *Gerya's* (2013) equivalent intermediate proto-transform model.

The morphological characteristics and faulting within the northern section of the GTF are similar to *Angelier et al.*'s (2004) stage three transform fault end-member and *Gerya's* (2013) intermediate stage proto-transform. *Angelier et al.*'s (2004) stage three, or mature transform, differs from earlier stages by the presence of a clearly defined strike-slip fault trace. No slip indicators, however, have

been observed at the GTF owing to a lack of detailed observations. The *Gerya* (2013) model expands upon this stage of transform evolution and predicts that proto-transforms between ~3 million years and ~4 million years old will be defined by ~5-7 km wide and ~1-3 km deep depressions connecting spreading centers; the northern section of the GTF is consistent with these model predictions (Figure 4B; ~10 km wide and ~1 km deep), but it is slightly wider. The deviation in TF width from model predictions may be due to the influence of the nearby plume or a result of TF elongation via ridge jumps (*Mittelstaedt et al.*, 2012).

The GTF is bounded on the east and west by plume-influenced GSC. At 90.8°W, the GTF is ~130-185 km east of the peak of plume-attributed geochemical enrichment along the GSC (~92°W) (*Schilling et al.*, 1982; *Verma and Schilling*, 1982; *Verma et al.*, 1983; *Schilling et al.*, 2003), and ridge-morphology on either side of the TF is similar to fast-spreading ridges (e.g., *Canales et al.*, 1997). The GTF was likely created by processes associated with plume-ridge interaction (e.g., *Hey*, 1977; *Wilson and Hey*, 1995; *Mittelstaedt et al.*, 2012). From its formation to present day, the GTF has likely been under the influence of the nearby plume. Intra-transform lavas may have plume-influenced compositions that can inform broader perspectives on plume-ridge interaction.

2 Analytical Methods

2.1 Major element compositions

Samples from the Galápagos Transform were prepared at Colgate University for X-ray fluorescence spectroscopy using a method adapted from *Norrish and Hutton* (1969). Rocks were chipped and picked to avoid alteration products and phenocrysts, then powdered in a tungsten carbide shatterbox following pre-contamination procedures. Rock powders were dried overnight at 60°C and then heated to 950°C for 3 hours to drive off volatiles. A precisely measured mass of each powder (0.5000 g ± 0.0003 g) was combined with 4.5000 g ± 0.0003 g of high purity lithium tetraborate, and then melted in a Claisse fluxer using platinum crucibles. The mixture was poured into platinum molds and cooled in air. Each glass disc was analyzed using a Philips PW2404 X-ray fluorescence spectrometer in batches of five samples along with a USGS Standard Reference Material (SRM) run as an unknown (BHVO-2) that was similarly prepared (Table 2) (*Wilson*, 1997).

2.2 Trace element compositions

Lavas were prepared for trace element analysis at Colgate University following dissolution methods adapted from *Harpp et al.* (2003). Each sample was chipped and picked to avoid alteration

products and phenocrysts, and then sonicated in purified water for a minimum of 15 minutes, until rinse water became clear. Once dried, samples were dissolved in a mixture of purified nitric and hydrofluoric acids (3:2 proportion by volume) and then evaporated in a HEPA-filtered laminar flow hood. Samples were then diluted 1000-fold with a 50-50 mixture of purified HNO3 and water.

Each solution was analyzed in triplicate on a Varian 820MS Inductively Coupled Plasma-Mass Spectrometer (ICP-MS). A suite of USGS SRMs (BCR-1, BHVO-2, W-2, DNC-1, and AGV-2; Table 3) was used as external calibration standards. A solution of USGS SRM W-2 was analyzed as an unknown every 5 samples to monitor precision and accuracy (Table 3). A 200 ppb in-line internal standard solution of 115In, 133Cs, 182W, and 205Tl was used to monitor instrument drift; analyte masses were corrected to the closest internal standard mass (*Eggins et al.*, 1997). For elements with atomic masses great than 89, precision was <4 % (1σ) in replicate W-2 solutions run as unknowns. For elements with atomic masses less than 89, precision was <8%, with the exception of Sc and Rb, which registered >8%.

A subset of samples (D2-1a, D2-5, and D2-7; major element analysis reported by *Sinton et al.* (2003)) was processed and analyzed at Washington State University's Geoanalytical Laboratory for trace element compositions on a ThermoFinnigan Neptune Multicollector-Inductively Coupled Plasma-Mass Spectrometer (MC-ICP-MS); methods, standards, and precision information are available at the Geoanalytical Laboratory website (http://www.sees.wsu.edu/Geolab/note/icpms.html).

2.3 Radiogenic isotopic ratios

Rocks D30C and D33A were prepared for radiogenic isotope analysis at the University of Florida following procedures adapted from *Harkins et al.* (2008). To remove surficial contamination from seawater, samples were leached with 2 mL of thrice distilled 6 N HCl per 100 mg of rock. The sample and acid combination was heated to 90˚C for 20 minutes, removed from heat and ultrasonicated for 10 minutes, then re-heated for 10 minutes and ultrasonicated for an additional 5 minutes. The remaining rock was then removed from acid and washed twice with purified H2O. After dissolution, Pb, Sr, and Nd were separated using ion exchange chromatography following the procedure of *Goss et al.*, (2010).

The Sr, Nd, and Pb separates from D30C and D33A were analyzed on the Nu-Plasma Multi-Collector Inductively Coupled Plasma-Mass Spectrometer (MC-ICP-MS) at the University of Florida.

Samples were diluted with 2% HNO3 to achieve ~4-6 V total ion current for each solution concentration. To monitor instrument performance, NBS 987 Sr and JNDi Nd standards were analyzed every 4 samples. Strontium compositions were normalized to NIST987 ($^{87}Sr/^{86}Sr$ = 0.710240); Nd results were normalized to La Jolla Nd ($^{146}Nd/^{144}Nd$ of 0.7219). The Pb analyses were normalized to NIST981 (*Todt et al.*, 1996). Long term Pb standard averages are $^{206}Pb/^{204}Pb$ = 16.938 ±4 (2σ), $^{207}Pb/^{204}Pb$ = 15.488 ±3 (2σ), and $^{208}Pb/^{204}Pb$ = 36.693 ±9 (2σ).

Samples D33C and D33A were analyzed for radiogenic isotope compositions at the University of Washington. Separation of Sr and Nd isotopes was performed following procedures from *Nelson* (1995). Mass spectrometry procedures for Sr are described in *Gaffney et al.* (2004) and procedures for Nd are described in *Gaffney et al.* (2007). Separation of Pb and multi-collector inductively coupled plasma mass spectrometer (MC-ICP-MS) analyses followed the procedure of *Harkins et al.* (2008). Handpicked glass and rock chips were leached with 2 mL of thrice distilled 6M HCl per 100 mg of rock and heated at 90˚C for 20 minutes to remove surficial seawater contamination. Afterwards, the mixture was ultrasonicated for 10 minutes, heated for an additional 10 minutes, ultrasonicated for 5 minutes and then rinsed twice with purified water. The samples were then dissolved in concentrated ultrapure HF and HNO3, dried, and redissolved in 1.0 N HBr. The solution was passed through columns of BioRad AG-1-X8 100-200 mesh anion exchange resin. To ensure purity, Pb was eluted twice with 6 M HCl. The remaining fraction was processed for Sr and Nd separation following *Nelson* (1995). Neodymium and Sm were separated with columns of HDEHP-coated Teflon beads and 0.14 M and 0.5 M HCl.

Ratios of Nd and Pb isotopes were analyzed on a Nu Plasma MC-ICP-MS at the University of Washington. Lead isotope ratios were corrected to an internal Tl spike (NIST SRM-997) and sample-standard bracketed with NIST 981 (*Harkins et al.*, 2008). Strontium isotope ratios were measured by thermal ionization mass spectrometry at the Univserity of Washington. Strontium and Nd isotope ratios were corrected for mass fractionation to 0.1194 and 0.7129 (exponential correction law; *Nelson*, 1995). Strontium compositions were normalized to NIST987 ($^{87}Sr/^{86}Sr$ = 0.710240); Nd results were normalized to La Jolla Nd ($^{146}Nd/^{144}Nd$ of 0.7219). External reproducibility (2σ) is: Nd = ± 30 ppm; Sr = ± 30 ppm; Pb = ± 125, 150, and 200 ppm for $^{206}Pb/^{204}Pb$, $^{207}Pb/^{204}Pb$, and $^{208}Pb/^{204}Pb$, respectively. The Pb analyses were normalized to NIST981 (*Todt et al.*, 1996).

2.4 Electron microprobe analysis of selected phenocrysts

Selected phenocrysts were analyzed for major element oxides using a Cameca Camebax electron microprobe at Washington State University. Analyses were performed with a beam diameter of 15-20 microns, current of 10 nA, and potential of 15 kV. Periodic monitoring and adjustment of counts compensated for sodium loss during measurement.

3 Results

Previous expeditions to the GTF collected samples at only two locations along its ~100 km length (G-PRIME; *Cushman et al.*, 2004 and MEGA-PRINT; *Kokfelt et al.*, 2005); we present geochemical analyses of a newly compiled set of intra-transform lavas (ITLs) from within the GTF valley, including unpublished analyses of material recovered during the MV1007 expedition (D30, D33, and TC4A; Figure 6, Table 1; *Mittelstaedt et al.*, 2012).

3.1 Petrography

Lavas D2-1, D2-5, D2-7, D30B, and D33A collected from within the transform valley have similar petrographic characteristics to each other. All have a glassy groundmass with abundant skeletal plagioclase feldspar microphenocrysts (~0.1 mm diameter) and few, small (~1 mm diameter) vesicles (Figure 7, A and B). All lavas contain phenocrysts of olivine (Figure 7, C and D); the coarsest olivine crystals (~1 mm) are subhedral, and most phenocrysts with diameters smaller than 1 mm are variably corroded along the crystal boundaries, some with visible melt inclusions (Figure 7 D). Plagioclase feldspar phenocrysts are present in all lavas, have skeletal textures, and are variably resorbed (Figure 7 D). Diameters of plagioclase feldspar phenocrysts vary from 1.5 mm to <0.1 mm in all samples except D30B, which contains plagioclase phenocrysts up to 6 mm in diameter. Clinopyroxene has been identified only in the groundmass of D2-1, D2-5, and D2-7.

3.2 Major element compositions

Lava compositions within the 90.8°W transform valley vary from 6.42 to 9.42 wt.% MgO with 9.61-12.11 wt.% FeO and 49.22-50.58 wt.% SiO2 (Figure 8, Table 5). The glasses have CaO contents between 11.62 and 13.15 wt.% and 14.20-15.87 wt.% Al2O3. The highest Al2O3 and lowest FeO abundances are associated with the highest MgO contents. Only one sample (D43) has >0.1 wt.% K2O; this lava has the lowest MgO (6.42 wt.%) and the highest TiO2 abundances at 2.19 wt.%; all other material recovered from the GTF has <1 wt.% TiO2.

We assign GTF samples to northern and southern groups, on the basis of divisions in major element chemistry (Figure 9) and crystallization history. The northern lavas (except D43) have >9.0 wt.% MgO, whereas southern lavas have 8.0-8.5 wt.% MgO. The northern group of lavas may be related to a common parent by shallow fractionation of plagioclase and olivine. Thermodynamic models from the MELTS family of algorithms (*Ghiorso et al.*, 2002) using D2 compositions as a parental magma and fractionating at ~1 kbar produces liquid lines of descent that roughly parallel compositions of northern GTF lavas in major elements (Figure 10) and are consistent with shallow fractionation of plagioclase and olivine. There is not enough variation in major element observations to approximate a liquid line of descent (LLD) relating southern lavas to each other by fractional crystallization.

Electron microprobe analyses of select phenocrysts suggest different crystallization histories for the northern and southern samples. Plagioclase phenocrysts in the northern samples have cores with average anorthite contents of ~0.92AN (n=7) and rims of ~0.85AN (n=6). Some olivine phenocrysts in the northern group are not in chemical equilibrium with their host melt, though the phenocrysts rims are in equilibrium with GTF lavas (Figure 11). Phenocryst cores from southern samples appear to be in chemical equilibrium with their rims and host lavas. Southern sample phenocrysts are not chemically zoned and likely crystallized from one magma body or in the presence of the same melt composition, unlike the northern phenocrysts, which have either experienced multiple crystallization events, crystallized within two different magma bodies, or resided in a magma chamber that was periodically injected with melt of a different composition.

3.3 Incompatible trace element compositions

Incompatible Trace Element (ITE) concentrations in GTF lavas are enriched or depleted by roughly one order of magnitude relative to Primitive Mantle (PM) concentrations (Figure 13) (*McDonough and Sun*, 1995). All GTF rocks have Rb and Pb depletions relative to PM, and have negative Pb anomalies. Sample D43 also has positive Ti, Ta, and Nb anomalies (~30, ~7, and ~6 times PM concentration, respectively), unlike the other GTF samples.

Lavas dredged from the GTF have rare earth element concentrations that define positively sloping curves when normalized to chondrite compositions (Figure 12, Table 6). For GTF rocks, light rare earth element (LREE) concentrations are ~3-10 times chondritic values (*McDonough and Sun*, 1995). Heavy rare earth elements (HREE) have a flat chondrite-normalized concentration curve and are uniformly enriched ~15-20 times over chondrites. Lava D30B is more depleted in La and Ce than

the other GTF samples, with a La concentration of 0.28 ppm (between 1 and 2 times chondritic values) and Ce of 2.65 ppm (about 4 times chondritic values). All of the samples have a negative Eu anomaly.

3.4 Radiogenic isotope ratios

Transform valley samples have εNd from 6.14-7.40 and $^{87}Sr/^{86}Sr$ from 0.702925 to 0.703320 (Table 7, Figure 14). Among these samples, $^{206}Pb/^{204}Pb$ varies from 18.736 to 18.974, $^{207}Pb/^{204}Pb$ from 15.523 to 15.576, and $^{208}Pb/^{204}Pb$ from 38.344 to 38.590 (Table 7, Figure 14). In addition to the distinct differences in major element compositions between northern and southern samples, northern lavas are more enriched in radiogenic Pb, Sr, and Nd than southern lavas (Figure 15).

4 Data Analysis

4.1 Principal Component Analysis

Since the last examination of Galápagos mantle end-members, there has been additional sampling of the Galápagos Archipelago and the GSC (e.g., *Schilling et al.*, 2003; *Sinton et al.*, 2003; *Cushman*, 2004; *Kokfelt et al.*, 2005; *Ingle et al.*, 2010), prompting review of the mantle components contributing to Galápagos lava chemistry. The primary goal of Principal Component Analysis with these new data is to determine what source material contributes to GTF lavas.

Principal Component Analysis (PCA) is a statistical method used to deduce the principal axes of variation of a multidimensional data set. The original data set is transformed onto a new orthonormal coordinate system whose axes represent the directions of greatest variation in the data set. The axes can be ordered by their significance to the data set's variability, thus reducing the dimensions required to describe maximum and minimum variation of the data (e.g., *Marriott*, 1974; *McKillup and Dyar*, 2010). Using PCA on a set of radiogenic isotope data can highlight mixing relationships between sources that may not have been apparent in the original data projection (e.g. *Staudigel et al.*, 1984; *Harpp and White*, 2001).

We perform PCA on $^{87}Sr/^{86}Sr$, $^{143}Nd/^{144}Nd$, $^{206}Pb/^{204}Pb$, $^{207}Pb/^{204}Pb$, and $^{208}Pb/^{204}Pb$ from Galápagos lavas using the same data set as *Harpp and White* (2001), merged with a compilation of more recent analyses (*Schilling et al.*, 2003; *Sinton et al.*, 2003; *Cushman et al.*, 2004; *Geist et al.*, 2005; *Kokfelt et al.*, 2005; *Gibson and Geist,* 2010; *Ingle et al.*, 2010; *Gibson et al.*, 2012; *Harpp et al.*, 2014a; *Harpp et al.*, 2014b; *Wilson et al.*, In Prep), and the new data from the GTF presented here, a

total of 239 samples (129 samples were available at the time of the *Harpp and White* (2001) analyses). Owing to the limited number of $^{3}He/^{4}He$ analyses for Galápagos rocks, this analysis does not consider $^{3}He/^{4}He$ ratios. Each data set was origin-centered and normalized by its standard deviation to account for the absolute differences between the isotope systems (*McKillup and Dyar*, 2010).

End-members were selected using the orientation of the axes of principal variation (eigenvectors) and constrained by mixing lines in isotope space (Table 8, Figure 16) (*Langmuir et al.*, 1978). The compositional end-members determined using PCA are broadly consistent with those of *Harpp and White* (2001), thus the same naming convention is adopted here: PLUME, DUM, FLO, and WD. Calculated mixing lines for these four components can account for ~95% of the isotopic variability observed in Galápagos lavas (Figure 16).

The first principal component is aligned approximately with an eigenvector between *Harpp and White's* (2001) PLUME and DUM sources and describes ~83% of the isotopic variability observed in the available Galápagos samples (Table 9). Relative to Harpp and White's (2001) results, our PLUME end-member is more enriched in radiogenic isotopes and our DUM end-member is more depleted (Figure 16). The DUM reservoir is most similar isotopically to rocks from Genovesa, though more depleted (Figure 16), whereas the PLUME end-member resembles compositions from Fernandina lavas (Figure 16). Fernandina and GTF compositions lie closest to the PLUME-DUM mixing line in isotope space (Figure 16) and have PCA scores that correspond to those end-members (Figure 17); all other Galápagos lavas are offset from the PLUME-DUM mixing line and require a contribution from at least one of the remaining two end-members to explain their compositions.

The second principal component accounts for ~10% of the isotopic variability in the Galápagos and defines an eigenvector between WD and FLO. Our proposed WD end-member is nearly identical to *Harpp and White's* (2001) WD. The WD end-member has $^{87}Sr/^{86}Sr$ and $^{143}Nd/^{144}Nd$ signatures (0.7029 and 0.5130, respectively) that fall between PLUME and DUM, but it is radiogenically enriched in all three Pb isotopes relative to PLUME (Figure 16). Our FLO end-member is more radiogenically enriched than previous estimates (*Harpp and White*, 2001) in all three isotope systems (Pb, Sr, Nd). It is also the most spatially restricted end-member; its contributions are strongest in Floreana lavas (Figure 16). The extreme isotopic enrichment in Floreana lavas is consistent with previous interpretations that this related compositions are influenced by recycled crustal component in the plume (*Harpp and White*, 2001; *Blichert-Toft and White*, 2001; *Gibson et*

al., 2012; *Harpp et al.*, in press). This argument is strengthened by the fact that mixing lines encompassing the Galápagos data set (Figure 16) require a two-fold increase in the concentrations of Pb and Sr relative to typical mantle concentrations.

In terms of Sr, Nd, and Pb isotopic ratios, the GTF lavas are compositionally most similar to Fernandina lavas, and lie on a mixing line between the amended DUM and PLUME end-members (Figure 16). Galápagos TF lavas are distinguished from GSC axial lavas and NGVP cones (Figure 16) by their lack of contributions from the WD end-member.

4.2 A mixing model for GTF lavas

To simplify our examination of the GTF lavas, we solve a set of equations that describe melt mixing between melts derived from two sources. Radiogenic isotope compositions of GTF lavas lie on a mixing line between PLUME and DUM sources, identified by PCA (Figure 15) and principal component scores show that FLO and WD sources do not contribute significantly to GTF lavas (Table 9). For these reasons, our model assumes that GTF lavas are a mixture of melts from two sources, an enriched, primitive source (PLUME) and a depleted source (DUM). Minor contributions from other sources are possible, but their isotope signatures are not clearly expressed. Our objective here is to investigate how much partial melt each source contributes to GTF lavas, constrained by trace element concentrations and radiogenic isotope ratios. The results of this model will help constrain source compositions that contribute to GTF lavas.

For our binary mixing model, we will assume that the enriched source is PLUME and the depleted source is DUM (Table 8), with radiogenic isotope ratios identified by PCA. For the DUM source, Sr and Nd concentrations are fixed at 6.092 ppm and 0.483 ppm from estimates of depleted mantle concentrations (*Workman and Hart*, 2005) (Table 10). We do not constrain Sr and Nd concentrations of the PLUME source as part of the initial conditions, which allows the model to predict a range of possible concentrations.

The model considers only Sr and Nd radiogenic isotope ratios and trace-element concentrations because measured Pb concentrations in GTF lavas are below instrument precision (Table 6). Our model assumes that melting occurs within the spinel stability field (<2 GPa) because there is no indication in trace element compositions that GTF lavas melted in the presence of garnet. The model also assumes that melting and mixing processes happen over a much shorter time scale than the half-life of radiogenic parents of Sr or Nd.

We do not consider solid-state mixing models because they yield unrealistic geochemical constraints to reproduce GTF lava chemistry, such as extents of melting in excess of 40% (e.g., *Niu*, 1997). Furthermore, previous studies indicate that solid-state mixing is unlikely in the upper mantle (e.g., *Farnetani and Richards*, 1995; *Ito et al.*, 1996, 1997; *Farnetani et al.*, 2002; *Ito*, 2003).

Using radiogenic isotope ratios and Sr and Nd concentrations, our mixing model constrains the relative volume fractions of contributions from PLUME and DUM to GTF melts in a two-component system. The model also constrains the degree of melting required to produce GTF lava compositions and the range of Sr and Nd concentrations in the PLUME source. A model that involves melting of an enriched (PLUME) and a depleted (DUM) source in which the melts first accumulate separately and then mix in a common reservoir (Figure 18) can be described by the following equations:

$$\boldsymbol{x} + \boldsymbol{y} = 1 \tag{1}$$

$$\boldsymbol{n}_{\mathbf{i}}' = \boldsymbol{n}_{\mathbf{i}}\boldsymbol{D}\mathbf{i} * (\mathbf{1} - \boldsymbol{F}_{\boldsymbol{d}})^{\frac{\mathbf{1}}{\boldsymbol{D}_{\mathbf{i}}} - \mathbf{1}} \tag{2}$$

$$\boldsymbol{m}_{\mathbf{i}}' = \frac{\boldsymbol{m}_{\mathbf{i}}}{\boldsymbol{D}_{\mathbf{i}}} * (\mathbf{1} - \boldsymbol{F}_{\boldsymbol{p}})^{\left(\frac{\mathbf{1}}{\boldsymbol{D}_{\mathbf{i}}} - \mathbf{1}\right)} \tag{3}$$

$$\boldsymbol{n}_{\mathbf{i}}'\boldsymbol{x} + \boldsymbol{m}_{\mathbf{i}}'\boldsymbol{y} = \boldsymbol{t}_{\mathbf{i}} \tag{4}$$

$$\boldsymbol{N}_{\mathbf{i}}\boldsymbol{n}_{\mathbf{i}}'\boldsymbol{x} + \boldsymbol{M}_{\mathbf{i}}\boldsymbol{m}_{\mathbf{i}}'\boldsymbol{y} = \boldsymbol{T}_{\mathbf{i}}\boldsymbol{t}_{\mathbf{i}} \tag{5}$$

Subscript *i* (=1 or 2) denotes references to strontium and neodymium, respectively, for any variable representing an elemental concentration ([Sr] or [Nd]) or isotopic ratio ($^{87}Sr/^{86}Sr$ or $^{143}Nd/^{144}Nd$). Variables *x* and *y* represent melt volume fractions contributed to the final melt, n_i' are the concentrations of radiogenic daughter elements in the DUM partial melt, n_i are DUM source concentrations, and the partial melt fraction for the DUM melt is F_d. In equations (3), (4), and (5), m_i' are the concentrations of elements in partial melts of the PLUME source and m_i are elemental concentrations in the PLUME source. Bulk partition coefficients are represented by D_i. In equation (5), T_i represents the radiogenic isotope ratios of transform lavas.

Equation (1) is the sum of melt fractions, which must always equal 1 (i.e., 100% of the contributing melts). Equation (2) describes fractional melting of the DUM source, and equation (3)

defines fractional melting of the PLUME source. Equation (4) describes the concentrations of incompatible trace elements in GTF melts, t_i. The radiogenic isotope ratio composition of GTF lavas, T_i, is calculated from equation (5) using the initial ratios of DUM and PLUME (N_i and M_i), weighted by the concentration of the element in each melt (n_i', m_i', t_i) and the contributing fraction, x and y.

The system of equations presented above to explain melt generation and mixing from two sources cannot be solved algebraically. Owing to its non-linearity (equations (2)-(3)) and the variability in constraints, such as mantle reservoir compositions and partition coefficients, this system of equations must be solved through iterative methods. To determine the range of admissible solutions constrained by the GTF data, we use a modified Metropolis-Hastings algorithm.

The Metropolis-Hastings algorithm (*Metropolis and Ulam*, 1949) is a Markov Chain Monte Carlo (random walk) method of sampling a probability distribution using a combination of model-specific and random rejection criteria to explore the space. Generally, the goal of the algorithm is to explore the entire model domain in a random walk from point to point (*Tarantola*, 2005). An initial random guess within the domain is given. From this initial point, a second guess is selected at random within the model bounds and evaluated using model-tuned probability criteria. If the probability evaluation is successful (i.e., if the random number associated with the guess satisfies the condition), the guess becomes the new initial point and the process is repeated. If the probability evaluation is unsuccessful, the algorithm does not advance, returns to the initial guess, and selects a new test guess in a random direction. Consequently, the Metropolis-Hastings algorithm has no memory (i.e., previous steps do not influence future steps; *Tarantola*, 2005). Given enough iterations and left unperturbed, the algorithm will explore the entirety of the model space. The model-tuned probability criteria prevent the algorithm from converging to a single solution without testing the entire model space; details on how model-tuned criteria were selected for our application are presented below.

We modify the Metropolis-Hastings algorithm to determine a location that minimizes the residual in the multi-dimensional space defined by equations (1)-(5). An initial point P0 (defined by the unknowns: x, y, m_i, m_i', n_i', F_p, F_d) is randomly selected from a multivariate normal distribution whose mean is the center of the model space (defined as the midpoint in the expected range of each input variable), with a standard deviation of 20% of the expected maximum variability in each variable (Table 10). The L_1 norm of the residuals for equations (1-5) is calculated using P_0 (where f_1 corresponds to the residual from equation (1), f_2 to equation (2), and so on):

$$\boldsymbol{L_{P_0}} = \sum_{\mathbf{1}}^{\mathbf{5}} |\boldsymbol{f_i}(\boldsymbol{P_0})| \quad (6)$$

A second point, P_{test}, is selected at random from another multivariate normal distribution with a standard deviation of 10% of the expected range of each variable and a mean centered on P_0. This small step size compared to the model domain assures that the algorithm makes evaluations between points that are relatively close to each other; too large a step size will make the algorithm encounter model boundaries more often than valid guesses within the domain. The L_1 norm of the residuals of equations (1-5) for the point P_{test} is calculated with equation (6). The following equation is then used to calculate the evaluation criterion C_{test} for the test point, P_{test}:

$$\boldsymbol{C_{test}} = \frac{\boldsymbol{L_{P_0} - kL_{P_{test}}}}{\boldsymbol{L_{P_0}}} \quad (7)$$

where C_{test} will always be <1. A random number, i, (between 0 and 1) is then compared to C_{test}. If C_{test} is greater than i, P_{test} becomes the new P_0 and the process is repeated. If C_{test} is less than i, Ptest is rejected, the algorithm returns to P_0 and a new P_{test} is selected. In this way, the algorithm will advance from points with a high residual to points with a lower residual, with some random probability of moving or not moving. The random rejection method assures that the algorithm tends toward guesses with lower residuals, but on occasion it will advance to guesses with higher residuals, reducing the chance that it will converge on a local, rather than a global, residual minimum.

Bounds on the model space are set to prevent the algorithm from seeking solutions to the system that are not physically plausible (i.e., negative concentrations or negative melt fractions). Variables x and y are restricted to values between zero and one. All other values are constrained to be positive.

The constant k is an empirical, model-dependent parameter; we choose k=0.75, because it is the largest value that consistently avoided local minima in the residuals without causing the algorithm to wander away from the absolute minimum in sensitivity tests. Larger values of k result in repeated convergence on a local minimum, even after 10^5 iterations. For lower values of k, the algorithm does not converge and moves randomly about the model space. Tuning k to an appropriate value ensures consistent random motion of the algorithm (*Tarantola*, 2005).

This adaptation of the Metropolis-Hastings algorithm does not provide a solution; rather it seeks the lowest residuals in the model space, which define a range of admissible solutions. By taking

many steps (10^6 here) and starting from multiple points (10^4 initial points), the algorithm converges on a distribution of solutions with minimized residuals. These points are binned into a hexagonal grid and reported as a probability distribution reflecting the number of points per bin (solution density; Figure 18). Areas of high solution density (dark colors in Figure 18) define the highest probability solutions to the melt-mixing model.

We can further reduce the range of admissible solutions by considering a subset bounded by geologic constraints (as opposed to purely mathematical constraints imposed by equations (1)-(5)) and restricting our discussion to solutions with the smallest residuals in equations (1)-(5). As described above, the model predicts ranges of PLUME source Sr and Nd concentrations up to 130 ppm and 13 ppm respectively, greater than six times estimated primitive mantle compositions (e.g., *McDonough and Sun*, 1995). Nevertheless, we limit our solution range to those that predict PLUME source Sr and Nd concentrations of 15-25 ppm Sr and 0.25-2.25 ppm Nd, using the primitive mantle compositions of ~19.9 ppm Sr and ~1.25 ppm Nd as a guide (*McDonough and Sun*, 1995). We further reduce this restricted range of admissible solutions to the top 10% of solutions with the smallest residuals from equations (1)-(5). A Student's T-test of each variable shows that the each variable in the adjusted solution distribution is statistically different from the unfiltered solution (Figure 18) and the initial guesses input into the Metropolis-Hastings algorithm.

The adjusted range of admissible solutions predicts that GTF lavas are produced by a ~0.68/0.32 (± 0.19) mixture of ~5% and ~3% partial melts of PLUME and DUM sources (Figure 19). As the volume of PLUME melt contribution increases, the degree of DUM partial melting loosens from ~3% to a range of ~2-5% (Figure 18). The extent of PLUME melting remains approximately constant (~4%) regardless of the relative proportions of DUM and PLUME material (Figure 18). Strontium and neodymium concentrations for each contributing melt from PLUME or DUM become more tightly constrained with larger volume contributions from their respective melt (Figure 18). No solutions with <0.20 PLUME or >0.80 DUM volume fractions fall within our restricted range of predictions (Figure 19).

5 Discussion

5.1 Melt generation by extension

Previous studies have shown that the lithospheric stress field in the northern Galápagos is influenced by the presence of the GTF (e.g., *Harpp and Geist*, 2002) and that lithospheric extension

may partially contribute to NGVP melt production (*Mittelstaedt et al.*, 2012). Melt may be produced at the GTF by a similar process of lithospheric extension. Using measurements of fault heave along two NE-SW oriented profiles, we estimate ~6.3 km of extension along a 25.5 km-long profile (strain of ~0.33) for the northern GTF section and ~7.8 km along a 25.5 km-long profile (strain of ~0.44) for the southern GTF section (Figure 20). *Mittelstaedt et al.* (2012) show that the northern GTF is ~2.5-3.5 million years old and the southern GTF is ~1 million years old. The different ages predicted for the northern and southern valleys suggest higher strain rates in the southern half of the transform since ~1 Ma. Using age constraints from *Mittelstaedt et al.* (2012), our measurements suggest extension rates of ~1.8-2.5 km Ma-1 across the northern GTF and ~7.8 km Ma-1 across the southern GTF, comparable to *Harpp and Geist*'s (2002) estimate of ~8 km Ma-1 based upon plate motions. On the basis of observations of fault populations surrounding the GTF (e.g., *Mittelstaedt et al.*, 2012), previous interpretations of melting mechanisms in the NGVP (*Harpp and Geist*, 2002), numerical models of melt production and extraction in the NGVP (*Mittelstaedt et al.*, 2012), and evidence for extension across the GTF (Figure 20), we propose that extensionally-driven decompression of mantle rocks is responsible for a portion of the melt generation beneath the GTF.

Melts produced by lithospheric extension experience small amounts of shallow fractionation before rising to the surface. Major element variation in Galápagos Transform lavas can be explained by shallow fractionation of plagioclase and olivine (Figure 8). The fine-grained groundmass texture of GTF basalts indicates that these melts did not stall in a magma chamber for long. Alternatively, any magma chamber that developed beneath the GTF was relatively short-lived. Disequilibrium between olivine phenocryst cores and rims in some GTF lavas implies that these phenocrysts crystallized within a melt body that received injections of new material of a different composition (Figure 11). This new material may have homogenized within a GTF magma chamber, as no observations other than phenocryst disequilibrium suggest multiple, comingled melts beneath the GTF. Once produced, these melts do not experience significant crystallization and likely ascended rapidly to the surface.

5.2 Mantle sources in the Galápagos and at the Galápagos Transform

Consistent with the results of *Harpp and White* (2001), our principal component analysis requires that at least four isotopically distinct mantle reservoirs contribute material to Galápagos lavas (Figure 16). Three of these components, DUM, PLUME, and WD, are expressed in lavas along the GSC and in the NGVP (Figure 16). The WD component, identified by elevated $^{207}Pb/^{204}Pb$ and

$^{208}Pb/^{204}Pb$ for a given $^{206}Pb/^{204}Pb$ (e.g., *Harpp and White*, 2001), is not detectable to a significant extent in lavas from the Galápagos Transform, however (Figure 20). This raises two questions: (1) what is the WD component, and (2) why is it not clearly expressed in GTF melts, despite its expression in along-axis GSC lavas?

5.3 The WD component

The WD isotopic end-member (*Harpp and White*, 2001) is characterized by elevated $^{207}Pb/^{204}Pb$ and $^{208}Pb/^{204}Pb$ for a given $^{206}Pb/^{204}Pb$ relative to lavas from the rest of the Galápagos (Figure 16). Elevated $^{207}Pb/^{204}Pb$ and $^{208}Pb/^{204}Pb$ signatures along the GSC reach a maximum at 91-92°W, and may indicate that the WD component is intrinsic to the Galápagos plume (*Schilling et al.*, 2003), or that the plume enables expression of the WD component (*Ingle et al.*, 2010). Consistent with the former interpretation, the WD signature is observed in accreted seamounts at Quepos, Costa Rica, suggesting that the WD component has been present in Galápagos plume lavas for at least 60-65 Ma (*Mamberti et al.*, 2003, *Hoernle et al.*, 2000).

Elevated Pb isotope signatures, such as those identifying the WD component, are derived from ancient sources (i.e., primitive mantle or recycled crustal or sediment packages; e.g., *Elliott et al.*, 1999; *Kelley et al.*, 2005), which have had a significant amount of time (> ~1 billion years) to develop radiogenic enrichment from parental elements. Although the location of material in the mantle responsible for the WD signature is difficult to constrain using available data, *Harpp and White* (2001) highlighted several possible sources for the $^{207}Pb/^{204}Pb$ and $^{208}Pb/^{204}Pb$ enrichments along the GSC and at the Wolf-Darwin Lineament, including delaminated subcontinental lithosphere in the upper mantle (*Hart et al.*, 1984) and subducted oceanic crust (*Schilling et al.*, 2003), possibly including recycled sediment entrained in the plume thermal upwelling (*Dupré and Allègre*, 1983). Each of these potential sources for Pb isotope enrichment have specific chemical characteristics that can be used to identify their contributions to mantle compositions.

Elevated $^{208}Pb/^{204}Pb$ and $^{207}Pb/^{204}Pb$ for a given $^{206}Pb/^{204}Pb$ in GSC samples is consistent with a recycled component in the GSC source that has experienced seafloor alteration and subduction. Using mass balance methods at the Mariana trench along with observations from ODP hole 801, *Kelley et al.* (2005) show that seafloor alteration leads to enrichment in U/Pb and subduction alteration of oceanic crust depletes U and Pb (estimated losses of ~58% Pb and ~54% U) relative to Th. These complex alteration processes may evolve to elevated $^{208}Pb/^{204}Pb$ and $^{207}Pb/^{204}Pb$ for a given $^{206}Pb/^{204}Pb$ within ~0.5 Ga (*Kelley et al.*, 2005).

Hydrothermal and seawater alteration preferentially enrich Th/Pb and, depending on oxidation state, U/Pb in oceanic crust (*Pietruszka et al.*, 2013), chemical signatures that can survive subduction processes (e.g., *Kelley et al.*, 2005). In addition, lead depletion is enhanced during subduction (*Pietruszka et al.*, 2013). Incompatible trace element variations in GSC lavas are consistent with a source enriched in Th and to a lesser degree U and depleted in Pb by these processes (Figure 22), which supports the possibility of a recycled, altered oceanic crust component in the GSC and NGVP melt source that may be responsible for the WD isotopic signature.

Lead isotope ratio enrichments along the GSC also correlate with enrichment in light and middle rare earth element ratios [La/Sm] and [Sm/Yb] (Figure 21). Enrichment in [La/Sm] and [Sm/Yb] is achieved by partial melting, during which lighter REEs preferentially partition early into the melt phase. Lavas with enrichment in light REEs and Pb isotopes indicate that the WD signature is most strongly expressed in low-degree melts at the ridge. In corner-flow models of mid-ocean ridge melt production (e.g., *Braun et al.*, 2000), the lowest degree melts form in the deepest part of the melt column. We therefore conclude that WD is likely more concentrated in lower degree melts from the base of the melting column under the GSC (~125 km; e.g., *Ito et al.*, 1997; *Ingle et al.*, 2010).

5.4 Source composition

Despite their proximity to WD-influenced lavas along the GSC, there is no significant evidence for a WD isotope signature in GTF lavas. The GTF lavas are also depleted in ITEs relative to GSC lavas and some NGVP lavas. Both of these observations imply that either the source or the melting conditions under the GTF are distinct from those under the NGVP and GSC, and that the WD component is either not in the GTF source or is somehow removed from GTF melts.

The GTF is bounded to the east and west by cones and seamounts that have radiogenic isotope compositions indicative of WD influence in the NGVP and along the GSC (*Hoernle et al.*, 2000; *Harpp and White*, 2001, *Harpp et al.*, 2014); we infer that the mantle sources of NGVP and GSC melts are similar. This source is likely heterogeneous at a small scale, and varied melting of these heterogeneities is responsible for the complex isotopic variability seen in GSC and NGVP lavas (e.g., *Ito and Mahoney*, 2005; *Ingle et al.*, 2010). The GTF lavas are compositionally consistent with contributions from PLUME and DUM sources, both of which are expressed in NGVP and GSC lavas. Models of plume-ridge interaction (e.g., *Ito et al.*, 1997; *Ito and Bianco*, 2014) suggest that the Galápagos plume deflects towards the GSC, pushing ambient mantle out of the way and spreading out beneath the thermal lithosphere. It is unlikely that there is a unique source of GTF melts, distinct

from the GSC and NGVP sources, located underneath the transform. Rather, the sources of GTF, NGVP, and near-transform GSC melts are probably similar to each other and the lack of WD expression in GTF lavas may be a function of melting processes specific to the TF.

To investigate melt source compositions, we developed a two-component mixing model constrained by radiogenic isotope and trace element observations (section 4.2). We use this model to constrain a range of estimates of the degree of melting of the mantle underlying the GTF, assuming that the WD component is not present in the GTF source. Our model predicts that GTF lavas are composed of ~4% pooled partial melts from PLUME and DUM sources (Figure 18), mixing in a ~0.68/0.32 PLUME/DUM volume ratio. Using our calculated estimates of extents of melting and assuming a pooled fractional melting mechanism, we can estimate a plausible range of REE concentrations for the mean GTF source (Figure 22). Our calculated mean TE composition for the source of GTF lavas is more depleted than estimates of typical upper mantle compositions (e.g., *Salters and Stracke*, 2004; *Workman and Hart*, 2005). This suggests that at least one of the two components (PLUME or DUM) in the GTF source is more depleted in REE than the upper mantle, although our model does not differentiate which component is anomalously depleted. The source of GTF lavas either contains a localized ultra-depleted component or it has experienced melt extraction prior to melting beneath the TF, leaving behind a depleted source.

5.5 Depleted lavas at other TFs

At other oceanic transforms, notably extensional transforms, ITE-depleted compositions are observed in intra-transform lavas (*Hékinian and Bideau*, 1995; *Perfit et al.*, 1996; *Wendt et al.*, 1999; *Tepley*, 2004). Hypotheses to explain these anomalous compositions at Siquieros, Garrett, and Raitt transforms (*Hékinian and Bideau*, 1995; *Perfit et al.*, 1996; *Wendt et al.*, 1999; *Tepley*, 2004) fall broadly into two categories: a) preferential extraction of compositionally depleted melts from a mantle source (e.g., *Hékinian and Bideau*, 1995) or b) extensionally-driven melting of previously depleted MORB residues (e.g., *Wendt et al.*, 1999).

Based on the presence of at least one transitional MORB (T-MORB) sample in the Garrett Transform, *Hékinian and Bideau* (1995) propose a complex melt extraction process beneath the transform that extrudes ITE-depleted lavas on the sea floor while more enriched melts freeze in the upper mantle or lower crust during ascent. This hypothesis is supported by observations of numerous wehrlitic and gabbroic impregnations of Garrett peridotites (*Cannat et al.*, 1990; *Hékinian et al.*, 1992), which suggest that the higher density of enriched melts causes them to stall and

crystallize during ascent under the transform. No T-MORBs have been sampled within the GTF valley, and existing observations are insufficient to identify peridotite impregnations in the transform.

Alternatively, *Wendt et al.* (1999) propose that ITE-depleted compositions of intra-transform lavas at the Garrett Transform are inherited from the mantle source of those lavas. They suggest that the mantle source previously experienced partial melting at the EPR axis, removing incompatible element-enriched heterogeneities and leaving behind an ITE-depleted residue. Trans-tension across the Garrett transform initiates opening of the transform valley and extensionally-driven decompression melting of this ITE-depleted residue, producing depleted lavas that are subsequently extruded in the transform valley (Figure 23; *Wendt et al.*, 1999). From observations of similarly depleted compositions of intra-transform volcanics at Siquieros and Raitt transforms (*Hékinian and Bideau*, 1995; *Perfit et al.*, 1996), *Wendt et al.* (1999) postulate that ITE-depletion relative to adjacent spreading axes may be characteristic of intra-transform lavas and that re-activated melting of depleted ridge residues may be a result of trans-tensional transform stress regimes, in agreement with the new GTF observations.

5.6 Selective removal of enriched components of the GTF source

When applied to GTF melts, the *Wendt et al.* (1999) hypothesis agrees with chemical observations; the GTF source may have experienced a prior melting event, depleting it in incompatible trace elements. If this is the case, small-scale mantle heterogeneities responsible for enriched isotope signatures along the GSC may also have been removed from the mantle during prior melting events. It is possible that these small-scale heterogeneities carry the WD isotope signature within the Galápagos plume. What remains of these heterogeneities in the GTF source may be volumetrically minimal and contributes little to the isotopic signature of GTF lavas.

Villagomez et al. (2014) conclude that multi-stage melting is the primary cause of ITE and radiogenic isotope variability in Galápagos lavas from observations of seismic tomography beneath the Galápagos Archipelago. Their study shows that material communication between the plume and the GSC occurs at depths >100 km within the mantle. They suggest that selective removal of material enriched in radiogenic isotopes occurs first in the plume stem at the onset of hydrous melting and again under the GSC. *Villagomez et al.* (2014) also argue that depleted melts erupted in the NGVP are sourced from a ridge-depleted residue and produced by local extension, similar to the process we invoke to explain GTF melt compositions. The WD component may have been stripped

from the GTF melt source during previous melting that occurred away from the TF at the GSC or deeper in the plume stem. We extend *Villagomez et al.*'s (2014) and *Wendt et al.*'s (1999) hypotheses to include GTF lavas which, on the basis of geochemical model results, indicate that the GTF source: (1) is depleted in incompatible trace-elements (section 6.2.2); (2) is depleted in the WD isotope component (section 5.2) relative to GSC lavas; and (3) likely experienced a prior melting event before melting beneath the transform.

5.7 Implications for plume-ridge interaction

The geochemistry of Galápagos Transform basalts indicates an ITE-depleted mantle source, with some evidence for a missing isotope signature. At the GSC, MORB compositions may be dominated by isotope and trace element signatures of enriched mantle heterogeneities. However, using the TF as a filter, we can characterize the chemistry of more depleted components in the mantle underneath the GSC. This may indicate that some mantle components in the northern Galápagos mantle are more readily melted than others, or that the TF-absent compositions are small in volume relative to other mantle components that are expressed in GTF lavas. Transform lavas sample a more depleted range of compositions in the mantle and may inform which depleted compositions directly related to the Galápagos plume are communicating with the GSC.

6 Conclusions

From the observations presented above, we conclude the following:

- The GTF lavas have radiogenic isotope ratios consistent with contributions from the PLUME and DUM sources, identified by PCA (*Harpp and White*, 2001).
- Our model predicts that GTF lavas are a 0.68/0.32 (± 0.2) mixture of ~4% partial melts of PCA-identified PLUME and DUM components.
- GTF lavas may be sourced from mantle that has experienced prior melt extraction, either underneath the Galápagos Archipelago or under the GSC (e.g., *Wendt et al.*, 1999; *Villagomez et al.*, 2014). Prior melting events have left behind a mantle depleted in incompatible trace elements and the WD isotope component. The WD component (*Harpp and White*, 2001) has an isotope and trace element signature consistent with a recycled slab.
- The geochemical signature of lavas erupted at MORs is frequently dominated by the mantle component that melts first. Transform lavas, however, have signatures of mantle

components that are left behind after ridge melting. In this way, transform lavas may be used to examine underlying mantle compositions which are not strongly expressed at ridges. In this case, GTF lavas are sourced from the more depleted compositions of the underlying mantle and possibly indicate the composition of depleted material derived from plume-ridge material communication.

7 References

Angelier, J., F. Bergerat, R. Stefansson, and M. Bellou (2008), Seismotectonics of a newly formed transform zone near a hotspot: Earthquake mechanisms and regional stress in the South Iceland Seismic Zone, *Tectonophysics*, *447*(1-4), 95–116, doi:10.1016/j.tecto.2006.07.016.

Angelier, J., R. Slunga, F. Bergerat, R. Stefansson, and C. Homberg (2004), Perturbation of stress and oceanic rift extension across transform faults shown by earthquake focal mechanisms in Iceland, *Earth Planet. Sci. Lett.*, *219*(3-4), 271–284, doi:10.1016/S0012-821X(03)00704-0.

Argus, D. F., R. G. Gordon, and C. DeMets (2011), Geologically current motion of 56 plates relative to the no-net-rotation reference frame, *Geochemistry, Geophys. Geosystems*, *12*(11), n/a–n/a, doi:10.1029/2011GC003751.

Asimow, P. D., & Langmuir, C. H. (2003). The importance of water to oceanic mantle melting regimes. *Nature*, *421*(6925), 815-820.

Atwater, T., and K. C. Macdonald (1977), Are spreading centers perpendicular to their transform faults?, *Nature*, *270*(5639), 715–719, doi:10.1038/270715a0.

Blichert-Toft, J., and W. White (2001), Hf isotope geochemistry of the Galapagos Islands, *Geochemistry, Geophys. Geosystems*.

Braun, M., G. Hirth, and E. Parmentier (2000), The effects of deep dampt melting on mantle flow and melt generation beneath mid-ocean ridges, *Earth Planet. Sci. Lett.*, *176*, 339–356.

Canales, J. P., Dunn, R. A., Ito, G., Detrick, R. S., & Sallarès, V. (2014). Effect of Variations in Magma Supply on the Crustal Structure of Mid-Ocean Ridges: Insights from the Western Galápagos Spreading Center. The Galapagos: A Natural Laboratory for the Earth Sciences, 204, 363.

Canales, J., and J. Dañobeitia (1997), Variations in axial morphology along the Galápagos spreading center and the influence of the Galápagos hotspot, *J. Geophys.*, *102*.

Canales, J., G. Ito, R. Detrick, and J. Sinton (2002), Crustal thickness along the western Galapagos Spreading Center and the compensation of the Galapagos hotspot swell, *Earth Planet. Sci.*, *203*, 311–327.

Cannat, M., and M. Seyler (1995), Transform tectonics, metamorphic plagioclase and amphibolitization in ultramafic rocks of the Vema transform fault (Atlantic Ocean), *Earth Planet. Sci. Lett.*, *133*, 283–298.

Cannat, M., Bideau, D., & Hébert, R. (1990). Plastic deformation and magmatic impregnation in serpentinized ultramafic rocks from the Garrett transform fault (East Pacific Rise). *Earth and Planetary Science Letters*, *101*(2), 216-232.

Christie, D., R. Werner, and F. Hauff (2005), Morphological and geochemical variations along the eastern Galápagos Spreading Center, *Geochemistry Geophys. Geosystems*, *6*(1), doi:10.1029/2004GC000714.

Cushman, B., J. Sinton, and G. Ito (2004), Glass compositions, plume-ridge interaction, and hydrous melting along the Galápagos Spreading Center, 90.5°W to 98°W, *Geochemistry Geophys. Geosystems*, *5*(8), doi:10.1029/2004GC000709.

Detrick, R. S., J. M. Sinton, G. Ito, J. P. Canales, M. D. Behn, T. Blacic, B. Cushman, J. E. Dixon, D. W. Graham, and J. J. Mahoney (2002), Correlated geophysical, geochemical, and volcanological manifestations of plume-ridge interaction along the Galápagos Spreading Center, *Geochemistry Geophys. Geosystems*, *3*(10), 1–14, doi:10.1029/2002GC000350.

Dupré, B., and C. J. Allègre (1983), Pb–Sr isotope variation in Indian Ocean basalts and mixing phenomena, *Nature*, *303*(5913), 142–146, doi:10.1038/303142a0.

Eggins, S. M., Woodhead, J. D., Kinsley, L. P. J., Mortimer, G. E., Sylvester, P., McCulloch, M. T., ... & Handler, M. R. (1997). A simple method for the precise determination of≥ 40 trace elements in geological samples by ICPMS using enriched isotope internal standardisation. *Chemical Geology*, *134*(4), 311-326.

Elliott, T., Zindler, A., & Bourdon, B. (1999). Exploring the kappa conundrum: the role of recycling in the lead isotope evolution of the mantle. *Earth and Planetary Science Letters*, *169*(1), 129-145.

Farnetani, C. G., B. Legras, and P. J. Tackley (2002), Mixing and deformations in mantle plumes, *Earth Planet. Sci. Lett.*, *196*(1-2), 1–15, doi:10.1016/S0012-821X(01)00597-0.

Farnetani, D. G., and M. a. Richards (1995), Thermal entrainment and melting in mantle plumes, *Earth Planet. Sci. Lett.*, *136*(3-4), 251–267, doi:10.1016/0012-821X(95)00158-9.

Fornari, D., D. Gallo, and M. Edwards (1989), Structure and topography of the Siqueiros transform fault system: Evidence for the development of intra-transform spreading centers, *Mar. Geophys. Res.*

Fox, P., and D. Gallo (1984), A tectonic model for ridge-transform-ridge plate boundaries: Implications for the structure of oceanic lithosphere, *Tectonophysics*, *104*, 205–242.

Gaffney, A. M., Nelson, B. K., & Blichert-Toft, J. (2004). Geochemical constraints on the role of oceanic lithosphere in intra-volcano heterogeneity at West Maui, Hawaii. *Journal of Petrology*, *45*(8), 1663-1687.

Gaffney, A. M., Blichert-Toft, J., Nelson, B. K., Bizzarro, M., Rosing, M., & Albarède, F. (2007). Constraints on source-forming processes of West Greenland kimberlites inferred from Hf–Nd isotope systematics. *Geochimica et Cosmochimica Acta*, *71*(11), 2820-2836.

Geist, D., W. White, and A. McBirney (1988), Plume-asthenosphere mixing beneath the Galapagos archipelago, *Nature*.

Gerya, T. V. (2013), Initiation of transform faults at rifted continental margins: 3D petrological-thermomechanical modeling and comparison to the Woodlark Basin, *Petrology*, *21*(6), 550–560, doi:10.1134/S0869591113060039.

Ghiorso, M. S., Hirschmann, M. M., Reiners, P. W., & Kress, V. C. (2002). The pMELTS: A revision of MELTS for improved calculation of phase relations and major element partitioning related to partial melting of the mantle to 3 GPa. *Geochemistry, Geophysics, Geosystems*, *3*(5), 1-35.

Gibson, S. a., and D. Geist (2010), Geochemical and geophysical estimates of lithospheric thickness variation beneath Galápagos, *Earth Planet. Sci. Lett.*, *300*(3-4), 275–286, doi:10.1016/j.epsl.2010.10.002.

Gibson, S. a., D. G. Geist, J. a. Day, and C. W. Dale (2012), Short wavelength heterogeneity in the Galápagos plume: Evidence from compositionally diverse basalts on Isla Santiago, *Geochemistry, Geophys. Geosystems*, *13*(9), doi:10.1029/2012GC004244.

Graham, D. W., D. M. Christie, K. S. Harpp, and J. E. Lupton (1993), Mantle plume helium in submarine basalts from the Galápagos platform., *Science*, *262*(5142), 2023–6, doi:10.1126/science.262.5142.2023.

Goss, A. R., Perfit, M. R., Ridley, W. I., Rubin, K. H., Kamenov, G. D., Soule, S. A., ... & Fornari, D. J. (2010). Geochemistry of lavas from the 2005–2006 eruption at the East Pacific Rise, 9 46′ N–9 56′ N: Implications for ridge crest plumbing and decadal changes in magma chamber compositions. *Geochemistry, Geophysics, Geosystems*, *11*(5).

Harkins, S., M. Appold, and B. Nelson (2008), Lead isotope constraints on the origin of nonsulfide zinc and sulfide zinc-lead deposits in the Flinders Ranges, South Australia, *Econ. Geol.*, 353–364.

Harpp, K. S., and W. M. White (2001), Tracing a mantle plume: Isotopic and trace element variations of Gala ´ pagos seamounts, *Geochemistry Geophys. Geosystems*, *2*(2000).

Harpp, K. S., D. J. Fornari, D. J. Geist, and M. D. Kurz (2003), Genovesa Submarine Ridge: A manifestation of plume-ridge interaction in the northern Galápagos Islands, *Geochemistry, Geophys. Geosystems*, *4*(9), doi:10.1029/2003GC000531.

Harpp, K. S., Geist, D., Koleszar, A. M., Christensen, B., Lyons, J., Sabga, M., & Rollins, N. (2014). The geology and geochemistry of Isla Floreana, Galápagos: A different type of late-stage ocean island volcanism. The Galápagos: A Natural Laboratory for the Earth Sciences, edited by K. Harpp et al., AGU, Washington, DC.

Harpp, K. S., Wirth, K. R., Teasdale, R., Blair, S., Reed, L., Barr, J., & Korich, D. (2014). Plume-Ridge Interaction in the Galápagos: Perspectives from Wolf, Darwin, and Genovesa Islands. The Galapagos: A Natural Laboratory for the Earth Sciences, 204, 285.

Harpp, K., and D. J. Geist (2002), Wolf–Darwin lineament and plume–ridge interaction in northern Galápagos, *Geochemistry Geophys. Geosystems*, *3*(11), doi:10.1029/2002GC000370.

Hart, S. R. (1984), A large-scale isotope anomaly in the Southern Hemisphere mantle, *Nature*, *309*(5971), 753–757, doi:10.1038/309753a0.

Hékinian, R., and D. Bideau (1995), Magmatism in the Garrett transform fault (East Pacific Rise near 13 27′ S), *J. Geophys. Res.*, *100*(94).

Hekinian, R., Bideau, D., Cannat, M., Francheteau, J., & Hebert, R. (1992). Volcanic activity and crust-mantle exposure in the ultrafast Garrett transform fault near 13 28′ S in the Pacific. *Earth and Planetary Science Letters*, *108*(4), 259-275.

Hey, R. (1977), Tectonic evolution of the Cocos-Nazca spreading center, *Geol. Soc. Am. Bull.*, (71003).

Hoernle, K., R. Werner, J. P. Morgan, D. Garbe-Schönberg, J. Bryce, and J. Mrazek (2000), Existence of complex spatial zonation in the Galápagos plume, *Geology*, (5), 435–438.

Hofmann, A. W., and W. M. White (1982), Mantle plumes from ancient oceanic crust, *Earth Planet. Sci. Lett.*, *57*(2), 421–436, doi:10.1016/0012-821X(82)90161-3.

Hooft, E. E. E., D. R. Toomey, and S. C. Solomon (2003), Anomalously thin transition zone beneath the Galápagos hotspot, *Earth Planet. Sci. Lett.*, *216*(1-2), 55–64, doi:10.1016/S0012-821X(03)00517-X.

Ingle, S., G. Ito, J. J. Mahoney, W. Chazey, J. Sinton, M. Rotella, and D. M. Christie (2010), Mechanisms of geochemical and geophysical variations along the western Galápagos Spreading Center, *Geochemistry Geophys. Geosystems*, *11*(4), doi:10.1029/2009GC002694.

Ito, G., & Bianco, T. (2014). Patterns in Galápagos Magmatism Arising from the Upper Mantle Dynamics of Plume-Ridge Interaction. The Galapagos: A Natural Laboratory for the Earth Sciences, 204, 245.

Ito, G., J. Lin, and C. Gable (1997), Interaction of mantle plumes and migrating mid-ocean ridges: Implications for the Galápagos plume-ridge system, *J. Geophys. Res. Solid Earth*, *102*, 403–417.

Ito, G., J. Lin, and C. W. Gable (1996), Dynamics of mantle flow and melting at a ridge-centered hotspot: Iceland and the Mid-Atlantic Ridge, *Earth Planet. Sci. Lett.*, *144*(1-2), 53–74, doi:10.1016/0012-821X(96)00151-3.

Ito, G., J. Lin, and D. Graham (2003), Observational and theoretical studies of the dynamics of mantle plume–mid-ocean ridge interaction, *Rev. Geophys.*, *41*(4), 1017, doi:10.1029/2002RG000117.

Ito, G., & Lin, J. (1995). Oceanic spreading center–hotspot interactions: constraints from along-isochron bathymetric and gravity anomalies. *Geology*, *23*(7), 657-660.

Jackson, M. G., S. R. Hart, A. E. Saal, N. Shimizu, M. D. Kurz, J. S. Blusztajn, and A. C. Skovgaard (2008), Globally elevated titanium, tantalum, and niobium (TITAN) in ocean island basalts with high 3 He/ 4 He, *Geochemistry Geophys. Geosystems*, *9*(4), Q04027, doi:10.1029/2007GC001876.

Kelley, K., T. Plank, L. Farr, J. Ludden, and H. Staudigel (2005), Subduction cycling of U, Th, and Pb, *Earth Planet. Sci. Lett.*, *234*(3-4), 369–383, doi:10.1016/j.epsl.2005.03.005.

Kokfelt, T., C. Lundstrom, K. Hoernle, F. Hauff, and R. Werner (2005), Plume–ridge interaction studied at the Galápagos spreading center: Evidence from 226Ra–230Th–238U and 231Pa–235U isotopic disequilibria, *Earth Planet. Sci. Lett.*, *234*(1-2), 165–187, doi:10.1016/j.epsl.2005.02.031.

Kurz, M., and D. Geist (1999), Dynamics of the Galapagos hotspot from helium isotope geochemistry, *Geochim. Cosmochim. Acta*, *63*(23), 4139–4156.

Langmuir, C., and R. V. Jr (1978), A general mixing equation with applications to Icelandic basalts, *Earth Planet. Sci. Lett.*

Lonsdale, P. (1989), Segmentation of the Pacific-Nazca Spreading Center, 1° N–20° S, *J. Geophys. Res.*, *94*.

Macdonald, K., P. Fox, and L. Perram (1988), A new view of the mid-ocean ridge from the behaviour of ridge-axis discontinuities, *Nature*.

Mamberti, M., H. Lapierre, D. Bosch, and E. Jaillard (2003), Accreted fragments of the Late Cretaceous Caribbean–Colombian Plateau in Ecuador, *Lithos*, *66*, 173–199.

Marriott, F. H. C. (1974), *The interpretation of multiple observations*, Academic Press.

McBirney, A. R. (1993), Differentiated rocks of the Galapagos hotspot, *Geol. Soc. London, Spec. Publ.*, *76*(1), 61–69, doi:10.1144/GSL.SP.1993.076.01.03.

McDonough, W., and S. Sun (1995), The composition of the Earth, *Chem. Geol.*, *2541*(94).

McKillup, S., and M. D. Dyar (2010), *Geostatistics Explained: An Introductory Guide for Earth Scientists*, Cambridge University Press.

McKenzie, D., & Onions, R. K. (1992). Partial Melt Distributions From Inversion Of Rare-Earth Element Concentrations (J Petrol, Vol 32, Pg 1021, 1991). *Journal Of Petrology*, *33*(6), 1453-1453.

Palme, H., & O'Neill, H. S. C. (2003). Cosmochemical estimates of mantle composition. *Treatise on geochemistry*, *2*, 1-38.

Meschede, M., and U. Barckhausen (2000), Plate Tectonic Evolution of the Cocos-Nazca Spreading Center, in *Proceedings of the Ocean Drilling Program*, vol. 170.

Metropolis, N., and S. Ulam (1949), The monte carlo method, *J. Am. Stat. Assoc.*, *44*(247), 335–341.

Mittelstaedt, E., Soule, S., Harpp, K., Fornari, D., McKee, C., Tivey, M., ... & Mello, C. (2012). Multiple expressions of plume-ridge interaction in the Galápagos: Volcanic lineaments and ridge jumps. *Geochemistry, Geophysics, Geosystems*, *13*(5).

Mittelstaedt, E., & Ito, G. (2005). Plume-ridge interaction, lithospheric stresses, and the origin of near-ridge volcanic lineaments. *Geochemistry, Geophysics, Geosystems*, *6*(6).

Mittelstaedt, E., Soule, A. S., Harpp, K. S., & Fornari, D. (2014). Variations in CrustalThickness, Plate Rigidity, and Volcanic Processes Throughout the Northern Galápagos Volcanic Province. The Galapagos: A Natural Laboratory for the Earth Sciences, 204, 263.

Morgan, W. (1971), Convection plumes in the lower mantle, *Nature*.

Nagle, A. N., R. C. Pickle, A. E. Saal, E. H. Hauri, and D. W. Forsyth (2007), Volatiles in Basalts From Intra-Transform Spreading Centers: Implications for Melt Migration Models, *AGU Fall Meet. Abstr.*, *-1*, 05.

Nelson, B. (1995), Fluid flow in subduction zones: evidence from Nd-and Sr-isotope variations in metabasalts of the Franciscan complex, California, *Contrib. to Mineral. Petrol.*

Niu, Y. (1997), Mantle Melting and Melt Extraction Processes beneath Ocean Ridges: Evidence from Abyssal Peridotites, *J. Petrol.*, *38*(8), 1047–1074, doi:10.1093/petroj/38.8.1047.

Norrish, K., and J. Hutton (1969), An accurate X-ray spectrographic method for the analysis of a wide range of geological samples, *Geochim. Cosmochim. Acta*.

Perfit, M., D. Fornari, and W. Ridley (1996), Recent volcanism in the Siqueiros transform fault: picritic basalts and implications for MORB magma genesis, *Earth Planet. Sci. Lett.*, *141*.

Pietruszka, A. J., M. D. Norman, M. O. Garcia, J. P. Marske, and D. H. Burns (2013), Chemical heterogeneity in the Hawaiian mantle plume from the alteration and dehydration of recycled oceanic crust, *Earth Planet. Sci. Lett.*, *361*, 298–309, doi:10.1016/j.epsl.2012.10.030.

Riedel, W. (1929), Zur mechanik geologischer brucherscheinungen, *für Mineral. Geol. und Paläontologie B*.

Saal, A. E., & Forsyth, D. W. (2004, December). MORB composition in intra-transform spreading centers: A key test of models of mantle flow and melt transport. In *AGU Fall Meeting Abstracts* (Vol. 1, p. 04).

Salters, V. J. M., and A. Stracke (2004), Composition of the depleted mantle, *Geochemistry, Geophys. Geosystems*, *5*(5), doi:10.1029/2003GC000597.

Schilling, J. (1991), Fluxes and excess temperatures of mantle plumes inferred from their interaction with migrating mid-ocean ridges, *Nature*.

Schilling, J., D. Fontignie, J. Blichert-Toft, R. Kingsley, and U. Tomza (2003), Pb-Hf-Nd-Sr isotope variations along the Galápagos Spreading Center (101–83 W): Constraints on the dispersal of the Galápagos mantle plume, *Geochemistry Geophys. Geosystems*, 4(10), doi:10.1029/2002GC000495.

Sinton, J., R. Detrick, J. P. Canales, G. Ito, and M. Behn (2003), Morphology and segmentation of the western Galápagos Spreading Center, 90.5°-98°W: Plume-ridge interaction at an intermediate spreading ridge, *Geochemistry, Geophys. Geosystems*, *4*(12), doi:10.1029/2003GC000609.

Sleep, N. H. (1990), Hotspots and Mantle Plumes, Some Phenomenology, *J. Geophys. Res.*, *95*, 6715–6736.

Small, C. (1995). Observations of ridge-hotspot interactions in the Southern Ocean. *Journal of Geophysical Research: Solid Earth (1978–2012)*, *100*(B9), 17931-17946.

Smith, D. K., and T. H. Jordan (1988), Seamount statistics in the Pacific Ocean, *J. Geophys. Res.*, *93*(B4), 2899, doi:10.1029/JB093iB04p02899.

Staudigel, H., A. Zindler, S. R. Hart, T. Leslie, C.-Y. Chen, and D. Clague (1984), The isotope systematics of a juvenile intraplate volcano: Pb, Nd, and Sr isotope ratios of basalts from Loihi Seamount, Hawaii, *Earth Planet. Sci. Lett.*, *69*(1), 13–29, doi:10.1016/0012-821X(84)90071-2.

Sykes, L. (1967), Mechanism of earthquakes and nature of faulting on the mid-oceanic ridges, *J. Geophys. Res.*, *72*(8).

Tarantola, A. (2005), *Inverse problem theory and methods for model parameter estimation*.

Tepley, F., C. Lundstrom, K. W. W. Sims, and R. Hekinian (2004), U-series disequilibria in MORB from the Garrett Transform and implications for mantle melting, *Earth Planet. Sci. Lett.*, *223*(1-2), 79–97, doi:10.1016/j.epsl.2004.04.010.

Todt, W., Cliff, R. A., Hanser, A., & Hofmann, A. W. (1996). Evaluation of a 202Pb–205Pb Double Spike for High-Precision Lead Isotope Analysis.*. *Earth processes: reading the isotopic code*, 429-437.

Verma, S., and J. Schilling (1982), Galapagos Hot Spot-Spreading Center System: 2. $^{87}SR/^{86}$ SR and large ion lithophile element variations (85° W-101° W), *J. Geophys. Res.*, *87*.

Verma, S., J. Schilling, and D. Waggoner (1983), Neodymium isotopic evidence for Galapagos hotspot-spreading centre system evolution, *Nature*.

Villagómez, D. R., D. R. Toomey, D. J. Geist, E. E. E. Hooft, and S. C. Solomon (2014), Mantle flow and multistage melting beneath the Galápagos hotspot revealed by seismic imaging, *Nat. Geosci.*, *7*(2), 151–156, doi:10.1038/ngeo2062.

Villagómez, D. R., D. R. Toomey, E. E. E. Hooft, and S. C. Solomon (2007), Upper mantle structure beneath the Galápagos Archipelago from surface wave tomography, *J. Geophys. Res.*, *112*(B7), B07303, doi:10.1029/2006JB004672.

Wendt, J. I., M. Regelous, Y. Niu, R. Hékinian, and K. D. Collerson (1999), Geochemistry of lavas from the Garrett Transform Fault: insights into mantle heterogeneity beneath the eastern Pacific, *Earth Planet. Sci. Lett.*, *173*(3), 271–284, doi:10.1016/S0012-821X(99)00236-8.

White, W. (1993), Petrology and geochemistry of the Galápagos Islands: Portrait of a pathological mantle plume, *J. Geophys.*, *98*.

Wilson, D., and R. Hey (1995), History of rift propagation and magnetization intensity for the Cocos-Nazca spreading center, *J. Geophys. Res.*, *100*(95).

Wilson, E.L. (In Prep), Geochemical evolution of Santa Cruz Island, Galápagos Archipelago.

Wilson, J. (1965), A new class of faults and their bearing on continental drift, *Nature*.

Wilson, S. (1997), United States Geological Survey Certificate of Analysis Basalt, Hawaiian Volcanic Observatory , BHVO-2.

Workman, R. K., & Hart, S. R. (2005). Major and trace element composition of the depleted MORB mantle (DMM). *Earth and Planetary Science Letters*, *231*(1), 53-72.

8 Tables

Table 1. Sampling stations

Dredge and towcam sampling locations within the GTF. A: dredge or towcam sampling during the FLAMINGO cruise (*Mittelstaedt et al.,* 2012). B: dredge recovered during G-PRIME cruise (*Cushman et al.,* 2004). C: dredge recovered during MEGA-PRINT cruise (*Kokfelt et al.,* 2005). See Figure 6 for sampling map.

Dredge/Towcam	Latitude	Longitude	Depth (mbsl)
D30[A]	1.37	-90.75	2318
D33[A]	1.55	-90.80	2752
TC4[A]	1.38	-90.77	Unknown
EWI0004-002[B]	1.59	-90.82	3210
SON0158-043[C]	1.65	-90.82	3302

Table 2. Major element XRF precision

Average (n=19) for SRM BHVO-2 and relative standard deviation percent, calculated for each oxide as: $100 * \frac{\sigma_{oxide}}{oxide\ concentration}$

Standard Reference Material	SiO_2	TiO_2	Al_2O_3	Fe_2O_3	MnO	CaO	MgO	Na_2O	K_2O	P_2O_5	Total
BHVO-2 Average (n=19)	49.38	2.78	13.04	12.62	0.17	11.56	7.33	2.08	0.5	0.26	99.72
RSD%	0.17	0.34	0.28	0.15	n/a	0.24	0.12	0.45	n/a	0.56	

Table 3. ICP-MS precision

Precision for standard reference material W-2, run as an unknown every 5 samples. Trace element data are given in parts per million (ppm).

SRM	La	Ce	Pr	Nd	Sm	Eu	Gd	Tb	Dy	Ho	Er	Tm	Yb	Lu	Hf	Ta	Pb	Th	U
W-2	10.61	23.13	3.04	12.[87]	3.33	1.09	3.66	0.61	3.81	0.8	2.24	0.33	2.02	0.3	2.29	0.49	7.65	2.16	0.5
RSD%	1.22	1.51	1.56	1.54	1.59	1.76	2.57	1.52	1.25	1.48	1.55	1.49	1.72	1.68	1.14	3.84	1.17	2.29	1.8

SRM	Sc	V	Cr	Co	Ni	Cu	Zn	Rb	Sr	Y	Zr	Nb	Ba
W-2	35.78	265	91.51	44.91	73.61	103.3	74.94	20.16	194.3	22.7	89.35	7.73	174
RSD%	2.57	2.3	2.51	2.24	2.94	2.44	1.67	1.58	1.68	1.59	1.7	1.24	1.7

Table 4. Radiogenic isotope precision

Precision for radiogenic isotope analyses. * indicates comparison to SRM NBS9[87]. All other analyses reported relative to UW SRM BCR-1 (N=5).

Standard	$^{87}Sr/^{86}Sr$	$^{143}Nd/^{144}Nd$	$^{206}Pb/^{204}Pb$	$^{207}Pb/^{204}Pb$	$^{208}Pb/^{204}Pb$
SRM	0.71024*	0.512632	18.5[87]	15.613	38.473
RSD	0.01*	0.2	1.6	2.6	3.3

Table 5. Major element compositions of GTF rocks

Major element oxide compositions reported as wt.%. A: Original analyses reported by *Cushman et al.* (2004). B: Original analyses reported by *Kokfelt et al.* (2005). T: FeO reported as FeO + Fe_2O_3.

Sample	SiO_2	TiO_2	Al_2O_3	FeO^T	MnO	MgO	CaO	Na_2O	K_2O	P_2O_5
D30A	50.53	0.90	14.40	10.88	0.19	8.35	12.96	1.59	0.02	0.06
D30B	49.86	0.91	14.24	11.13	0.20	8.41	13.15	1.93	0.02	0.06
D30C	50.01	0.91	14.41	11.08	0.21	8.45	12.82	1.91	0.03	0.07
D33A	49.81	0.84	15.48	10.14	0.17	9.11	12.69	1.60	0.02	0.05
D33C	49.22	0.85	15.60	10.21	0.17	9.42	12.51	1.[86]	0.02	0.06
TC4A	50.58	0.99	14.45	11.15	0.21	8.20	12.47	1.73	0.03	0.07
EWI0004-002-001[A]	49.50	0.80	15.85	9.75	0.18	9.32	12.76	1.74	0.03	0.06
EWI0004-002-002[A]	49.54	0.80	15.82	9.71	0.17	9.25	12.73	1.73	0.02	0.06
EWI0004-002-003[A]	49.53	0.81	15.83	9.78	0.18	9.29	12.75	1.71	0.04	0.05
EWI0004-002-004[A]	49.47	0.83	15.84	9.79	0.17	9.30	12.77	1.72	0.03	0.06
EWI0004-002-005[A]	49.48	0.82	15.79	9.75	0.18	9.28	12.79	1.73	0.03	0.06
EWI0004-002-006[A]	49.58	0.82	15.87	9.66	0.17	9.26	12.65	1.71	0.02	0.05
EWI0004-002-007[A]	49.63	0.81	15.81	9.61	0.18	9.15	12.66	1.73	0.03	0.05
EWI0004-002-008[A]	49.51	0.80	15.85	9.69	0.18	9.27	12.69	1.72	0.03	0.05
EWI0004-002-009[A]	49.65	0.83	15.78	9.64	0.18	9.04	12.70	1.74	0.03	0.05
SON0158-043[B]	49.51	2.19	14.20	12.11	0.19	6.42	11.62	2.97	0.28	0.22

Table 6. Incompatible trace-element compositions of GTF lavas

Compositions reported as parts per million (ppm).

Sample	Rb	Ba	Th	U	K	Nb	Ta	Sr	Nd	Zr	Hf	Sm	Ti	Tb	Y	Yb
D30B	ND	ND	0.12	0.04	157.88	0.78	0.07	46.09	4.51	40.83	1.20	1.85	5433.38	0.58	26.93	2.79
D30C	0.25	ND	0.06	0.02	222.54	0.73	0.07	32.47	3.97	36.33	1.12	1.78	5478.94	0.54	25.78	2.71
D33C	0.19	ND	0.06	0.01	145.22	0.69	0.06	40.79	4.02	36.48	1.09	1.72	5072.68	0.52	23.61	2.46
D30A	0.27	ND	0.07	0.02	190.52	0.76	0.07	33.31	4.09	37.60	1.15	1.83	5376.11	0.56	26.77	2.79
D33A	0.23	ND	0.06	0.02	159.90	0.75	0.07	42.82	4.18	37.58	1.13	1.78	5052.00	0.53	24.29	2.54
D2-1b	1.65	7.05	0.19	0.09	ND	0.97	0.07	49.88	4.49	36.30	1.18	1.87	ND	0.57	22.91	2.44
D2-5	0.77	6.23	0.10	0.03	ND	0.89	0.07	50.32	4.23	35.44	1.16	1.83	ND	0.57	22.66	2.41
D2-7	0.55	5.27	0.09	0.08	ND	0.85	0.06	48.70	4.14	35.65	1.15	1.82	ND	0.57	22.81	2.47

Sample	La	Ce	Pr	Nd	Sm	Eu	Gd	Tb	Dy	Ho	Er	Tm	Yb	Lu
D30B	0.28	2.65	0.75	4.51	1.85	0.66	2.80	0.58	4.05	0.95	2.79	0.46	2.79	0.44
D30C	0.88	3.11	0.64	3.97	1.78	0.64	2.43	0.54	3.85	0.90	2.65	0.43	2.71	0.42
D33C	0.90	3.25	0.67	4.02	1.72	0.63	2.41	0.52	3.56	0.83	2.44	0.38	2.46	0.38
D30A	0.91	3.23	0.66	4.09	1.83	0.66	2.53	0.56	3.98	0.93	2.75	0.44	2.79	0.43
D33A	0.96	3.45	0.70	4.18	1.78	0.65	2.47	0.53	3.68	0.85	2.49	0.40	2.54	0.39
D2-1b	1.10	3.65	0.68	4.14	1.82	0.73	2.84	0.57	4.04	0.91	2.59	0.39	2.47	0.40
D2-5	1.20	3.82	0.72	4.23	1.83	0.75	2.82	0.57	4.01	0.92	2.59	0.38	2.41	0.41
D2-7	1.48	4.37	0.77	4.49	1.87	0.74	2.87	0.57	3.99	0.91	2.58	0.39	2.44	0.40

Table 7. Radiogenic isotope whole rock compositions of GTF lavas

Radiogenic isotope compositions of GTF whole-rock samples. A: The $^{87}Sr/^{86}Sr$ composition of D30C may be affected by seawater contamination, suggesting that the rock was insufficiently leached in acid before analysis (see text for procedure details).

Sample	$^{87}Sr/^{86}Sr$	$^{143}Nd/^{144}Nd$	$^{206}Pb/^{204}Pb$	$^{207}Pb/^{204}Pb$	$^{208}Pb/^{204}Pb$
D2-1	0.702925	0.513017	18.74	15.52	38.34
D30A	0.702992	0.512958	18.97	15.58	38.59
D33C	0.703048	0.512965	18.85	15.53	38.51
D33A	0.703122	0.512953	18.84	15.54	38.53
D30C	0.703320[A]	0.512990	18.76	15.53	38.40

Table 8. Radiogenic isotope compositions of PCA-derived end-members

Radiogenic isotope composition of Galápagos end-members were derived by PCA and constrained by mixing lines in isotope space.

End-member	$^{87}Sr/^{86}Sr$	$^{143}Nd/^{144}Nd$	$^{206}Pb/^{204}Pb$	$^{207}Pb/^{204}Pb$	$^{208}Pb/^{204}Pb$
DUM	0.7023	0.5132	17.70	15.42	37.26
PLUME	0.7039	0.5128	19.51	15.53	39.25
WD	0.7029	0.5130	19.67	15.79	39.76
FLO	0.7046	0.5126	21.31	15.84	41.50

Table 9. Principal component eigenvector significance

Percent of variability in the Galápagos isotope data set accounted for by each principal component

	PC1	PC2	PC3	PC4	PC5
Percent significance	83.0	10.1	3.66	2.74	0.56

Table 10. Input variables for Metropolis-Hastings melt mixing model

Values are given for all variables and constants used in the Metropolis-Hastings melt mixing model. (*) indicates a variable that is iteratively solved for from a multivariate normally distributed initial guess with a standard deviation (σ); a) estimated enriched upper mantle concentration from *Workman and Hart,* (2005); b) mean value calculated from transform analyses (n=5); c) source isotope ratio derived from PCA; d) estimated bulk partition coefficient for spinel peridotite melting (*McKenzie and O'Nions,* 1991).

Variable	**Definition**	**Value**	**Estimated variability (σ)***
x	Mixing fraction of depleted melt	0.50*	0.20
y	Mixing fraction of enriched melt	0.50*	0.20
m_1	Concentration of Sr in enriched source	20*	10.0
m_2	Concentration of Nd in enriched source	1.0*	0.50
m_1'	Concentration of Sr in enriched melt	35*	10.0
m_2'	Concentration of Nd in enriched melt	2.0*	0.75
n_1'	Concentration of Sr in depleted melt	10*	5.00
n_1'	Concentration of Nd in depleted melt	1.5*	0.50
F_p	Degree of melt of enriched source	0.10*	0.05
F_d	Degree of melt of depleted source	0.10*	0.05
n_1	Concentration of Sr in depleted source	6.092[a]	-
n_2	Concentration of Nd in depleted source	0.483[a]	-
t_1	Mean concentration of Sr in GTF melts	43.41[b]	-
$t2$	Mean concentration of Nd in GTF melts	4.19[b]	-
$T1$	Mean $^{87}Sr/^{86}Sr$ of GTF melts	0.70302[b]	-
$T2$	Mean $^{143}Nd/^{144}Nd$ of GTF melts	0.51393[b]	-

Table 10. (continued)

Variable	Definition	Value	Estimated variability (σ)*
N_1	$^{87}Sr/^{86}Sr$ of DUM source	0.7023[c]	-
N_2	$^{143}Nd/^{144}Nd$ of DUM source	0.5132[c]	-
M_1	$^{87}Sr/^{86}Sr$ of PLUME source	0.7039[c]	-
M_2	$^{143}Nd/^{144}Nd$ of PLUME source	0.5128[c]	-
D_1	Bulk partition coefficient of Sr	0.0150[d]	-
D_2	Bulk partition coefficient of Nd	0.0120[d]	-

9 Figures

Figure 1: Location map. Blue lines indicate plate boundaries, Nazca, Cocos, and Pacific plate motion vectors (NNR-MORVEL 56 reference frame) are indicated with arrows.

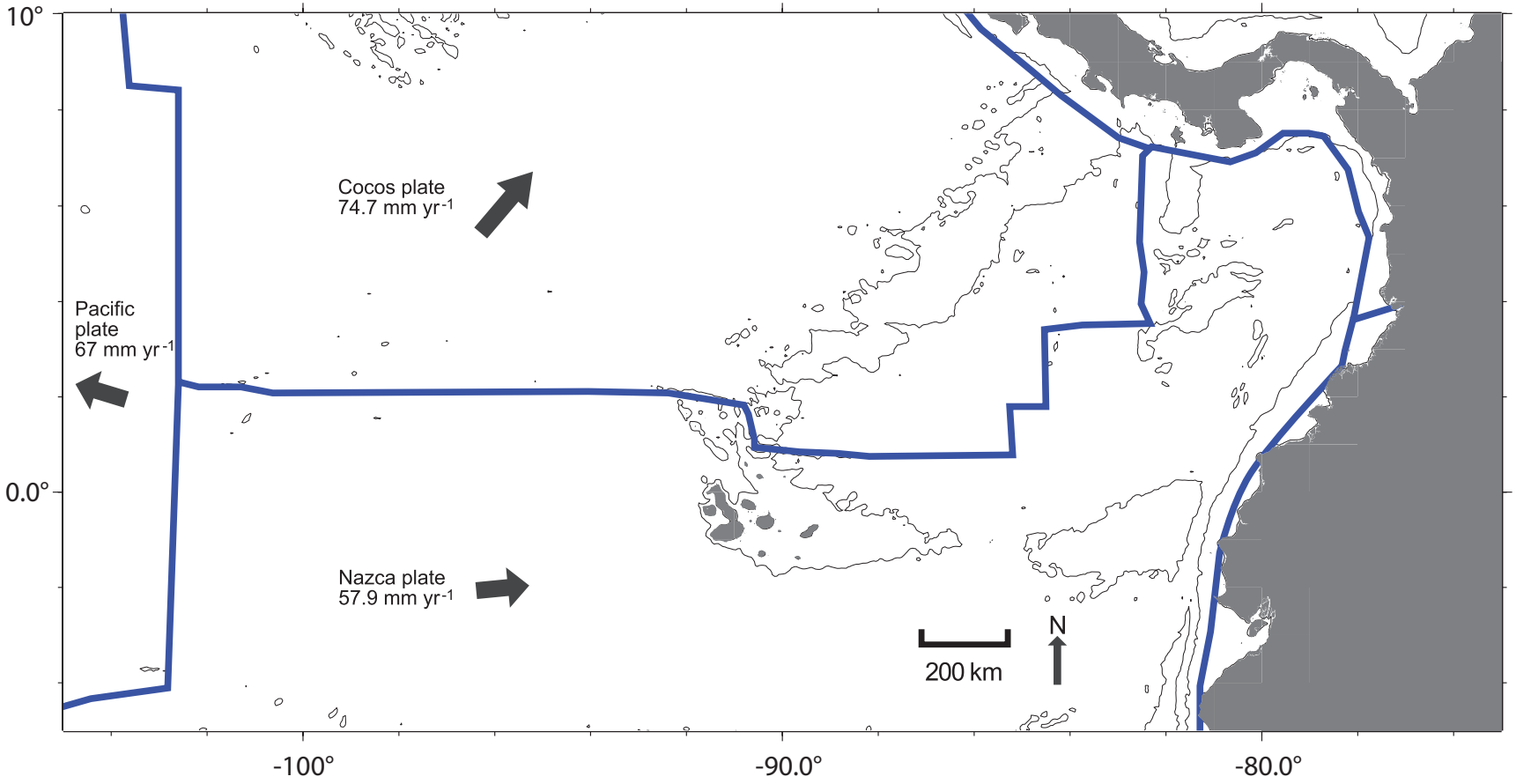

Figure 2. Bathymetry map of the GSC and Galápagos Archipelago with along-axis depth profile (A) and across-axis depth profiles (B, C, D, E). The GSC transitions from axial-valley (B, E) to axial ridge (C, D) morphology closer to the Galápagos Archipelago as a result of bathymetric swell caused by the Galápagos plume (e.g., Canales et al., 1997).

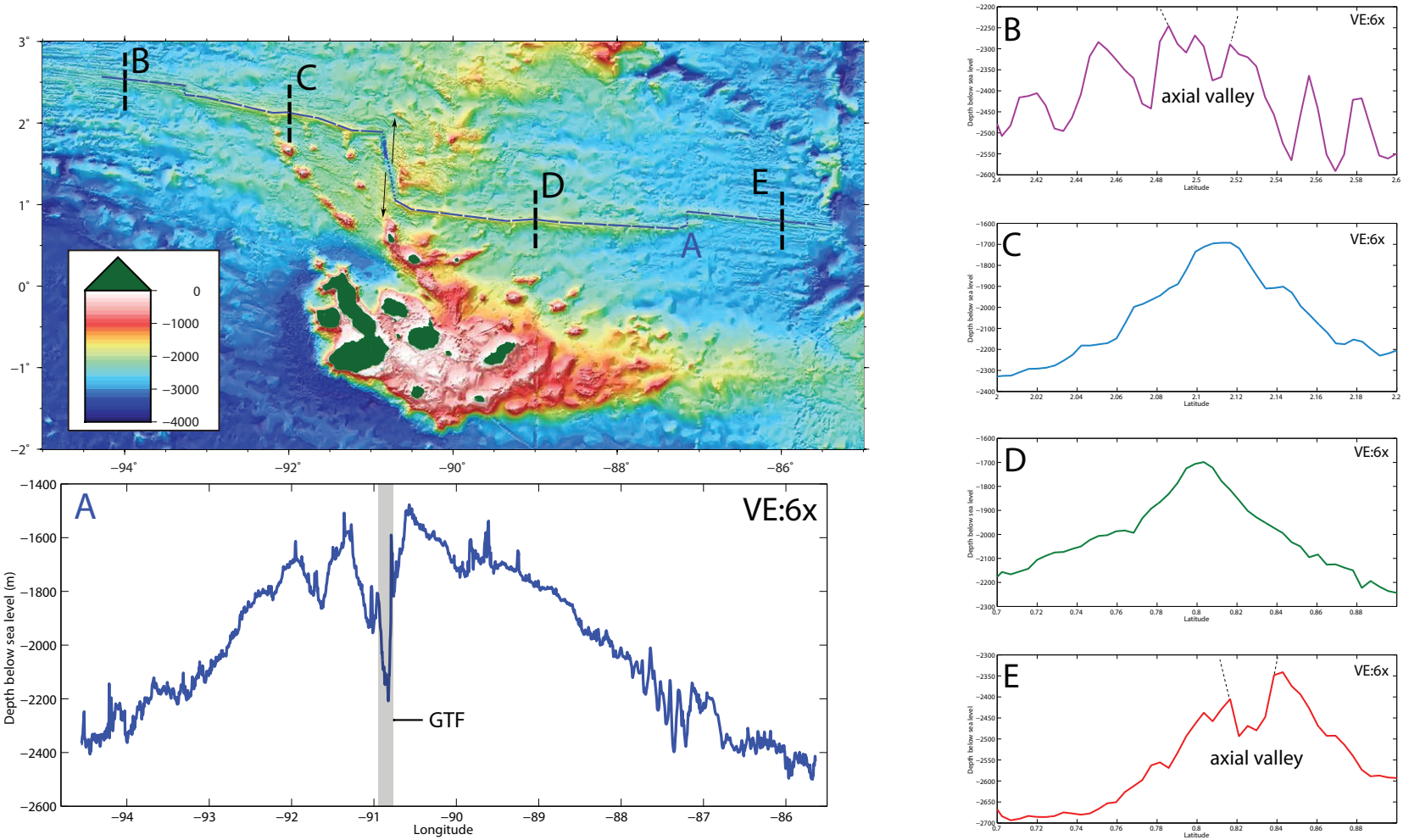

Figure 3. Radiogenic isotope ratios of GSC axial samples east and west of the Galápagos Archipelago. (Schillinget al., 1982; Verma and Schilling 1982; Verma et al., 1983; Detrick, 2002; Schillinget al., 2003; Cushmanet al., 2004; Christie et al., 2005; Kokfelt, 2006; Ingle et al., 2010). Radiogenic isotope enrichment is maximized at ~92°W. Away from ~92°W, radiogenic isotope ratios become more MORB-like.

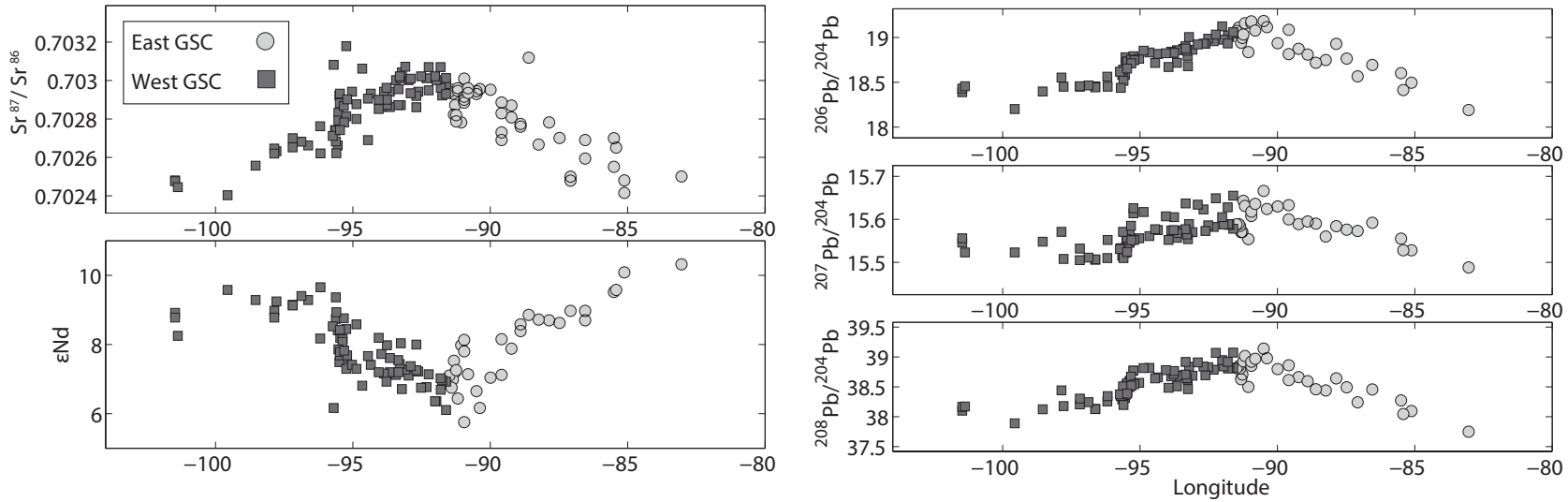

Figure 4. Morphology of the Galápagos Transform Fault. A: Northern GTF basin and cross profile. B: Southern GTF basin and cross profile. The southern GTF basin is wider and shallower than the northern GTF basin.

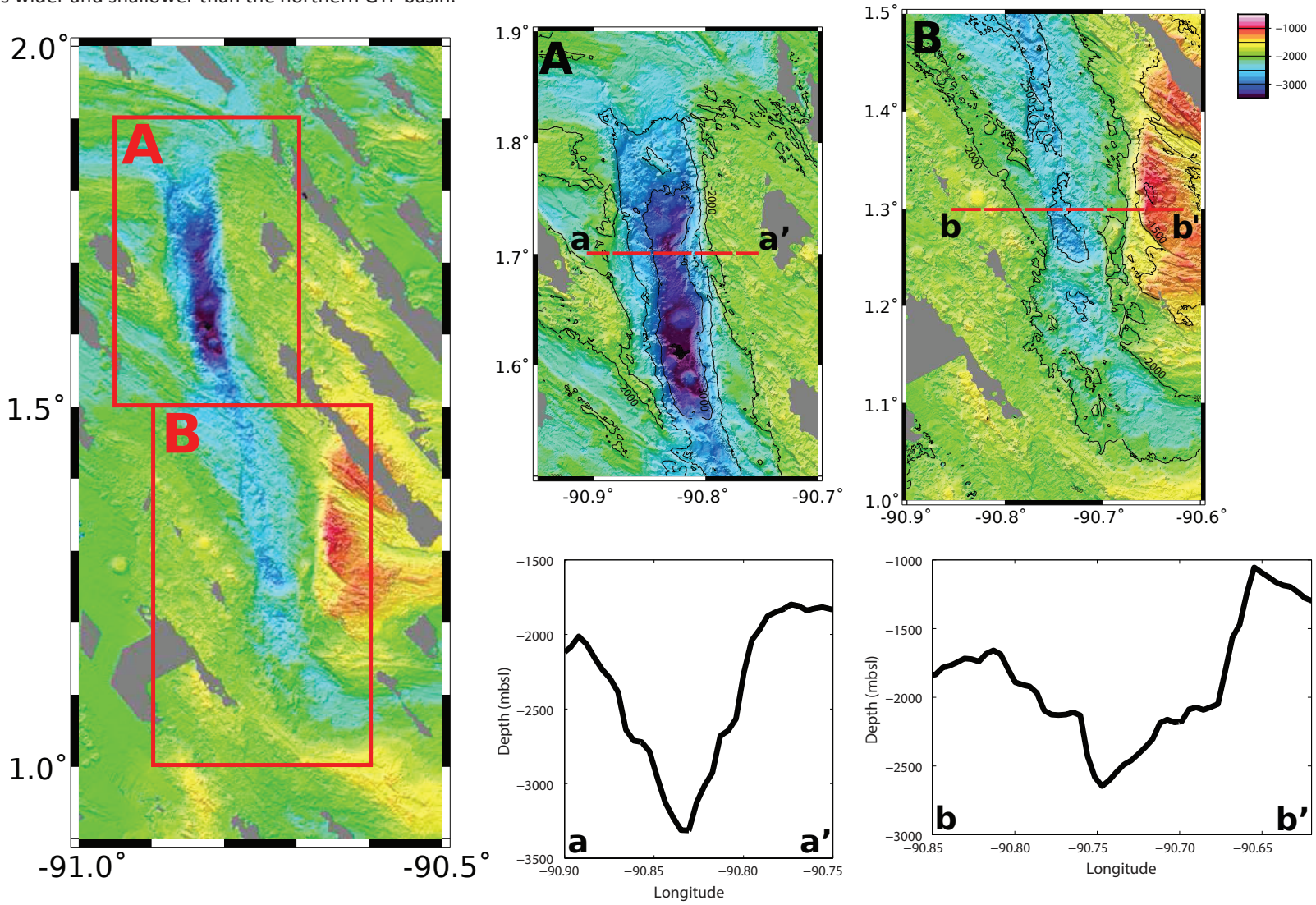

Figure 5. Reconstruction of Galápagos ridge jumps since ~5 Ma, after Mittelstaedt et al. (2012). Reference frame is the GTF (solid and dashed double line), with plume (pink circle) relative motion from east to west according to Nazca Plate motion and relative motion south equal to half-spreading rate of the GSC (Wilson and Hey, 1995). Ridge (solid black lines) jumps and corresponding lineaments (dashed lines) are numbered. The GTF (dashed double line) forms at ~2.5 Ma as a result of ridge jump (4) and is extended at ~1 Ma by ridge jump (5). Volcanic lineaments (bold black lines) develop due to plume-ridge interaction (e.g. Mittelstaedt et al., 2012). See text for further details.

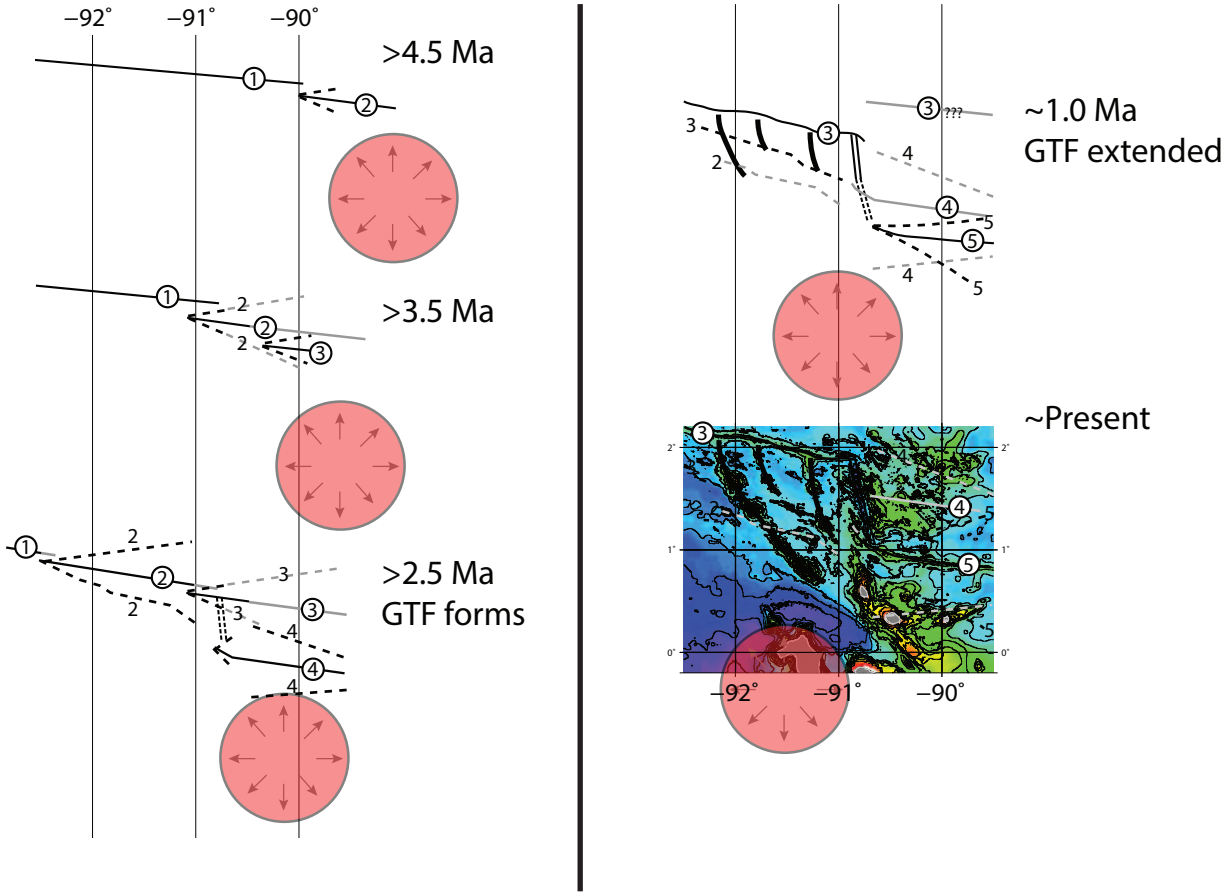

Figure 6. Dredge and tow-cam sampling locations. D30, D33, and TC4A were recovered during the MV1007 cruise (Mittelstaedt et al., 2012). Sample D2 was recovered during the G-PRIME cruise (Cushman et al., 2004). Sample D43 was recovered during the MEGA-PRINT cruise (Christie et al., 2005).

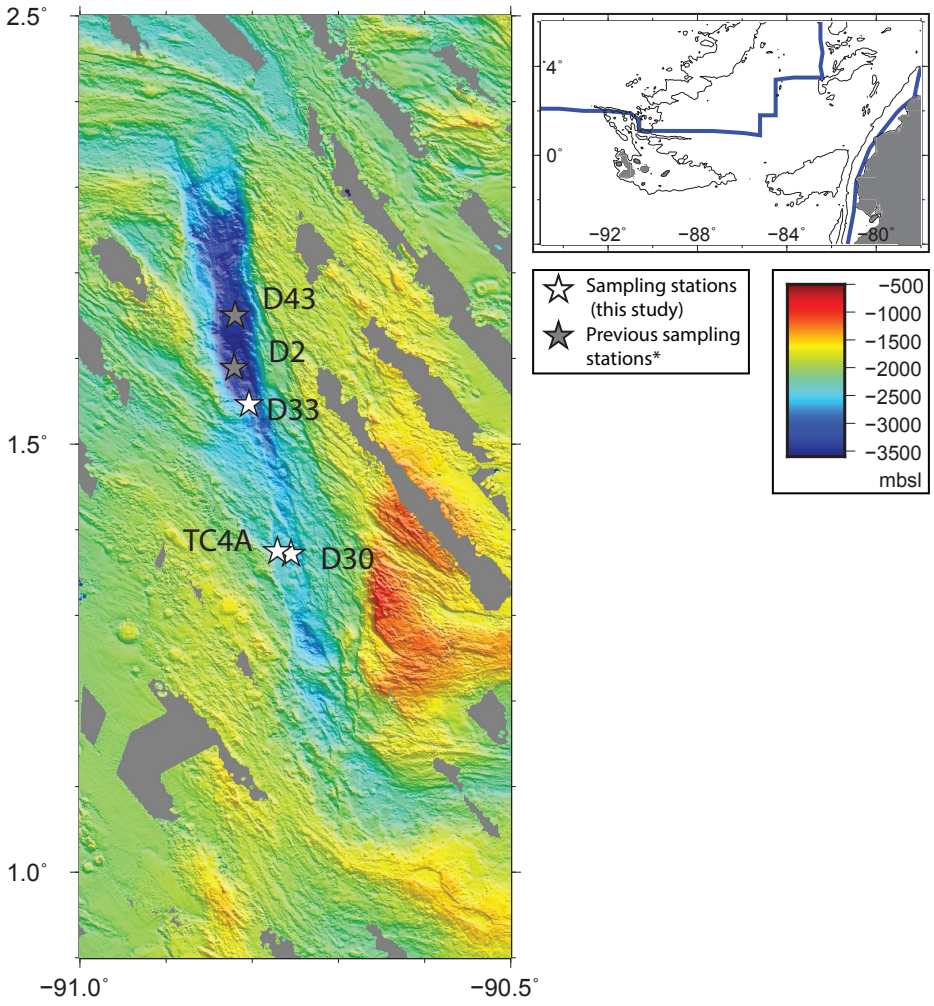

Figure 7. Photomicrographs of representative GTF samples. (A) Full section showing groundmass texture and phenocrysts; (B) Groundmass texture in cross-polarized light; (C) Olivine and (D) olivine with plagioclase phenocrysts in cross-polarized light.

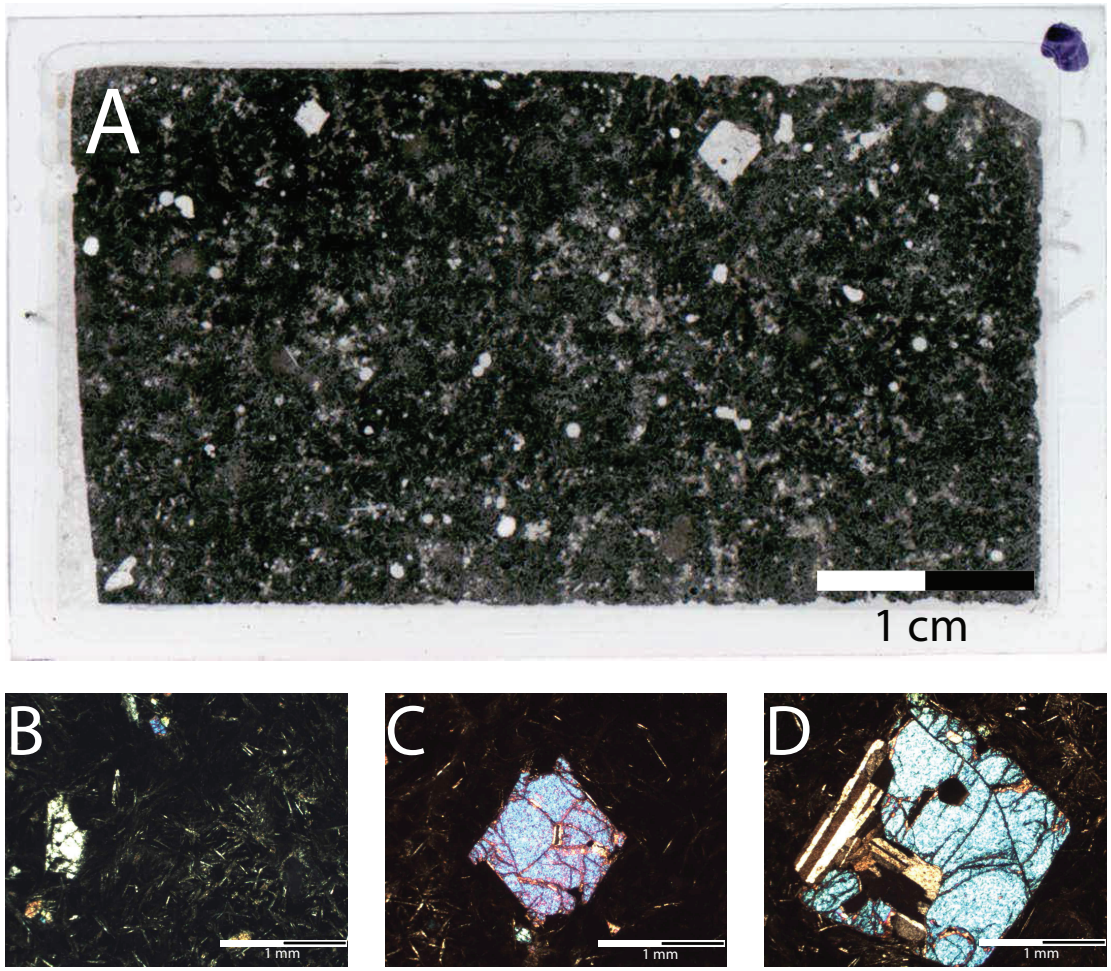

Figure 8. GTF major element oxide data. FeO^T calculated as $FeO+Fe_2O_3$. Symbols are larger than 2σ precision, except where indicated.

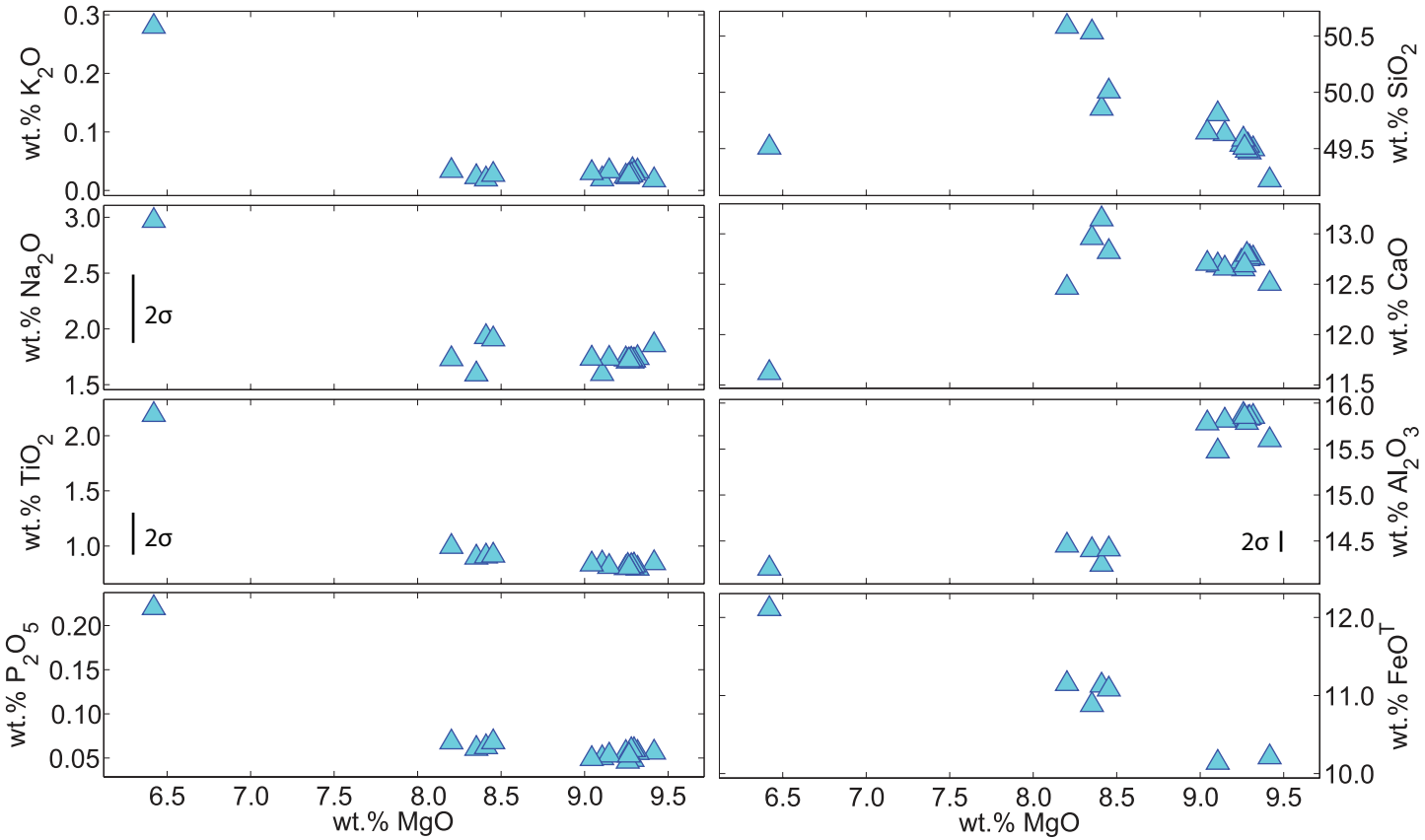

Figure 9. MgO, TiO_2, and CaO/Al_2O_3 whole rock major element oxide variation with latitude in the GTF.

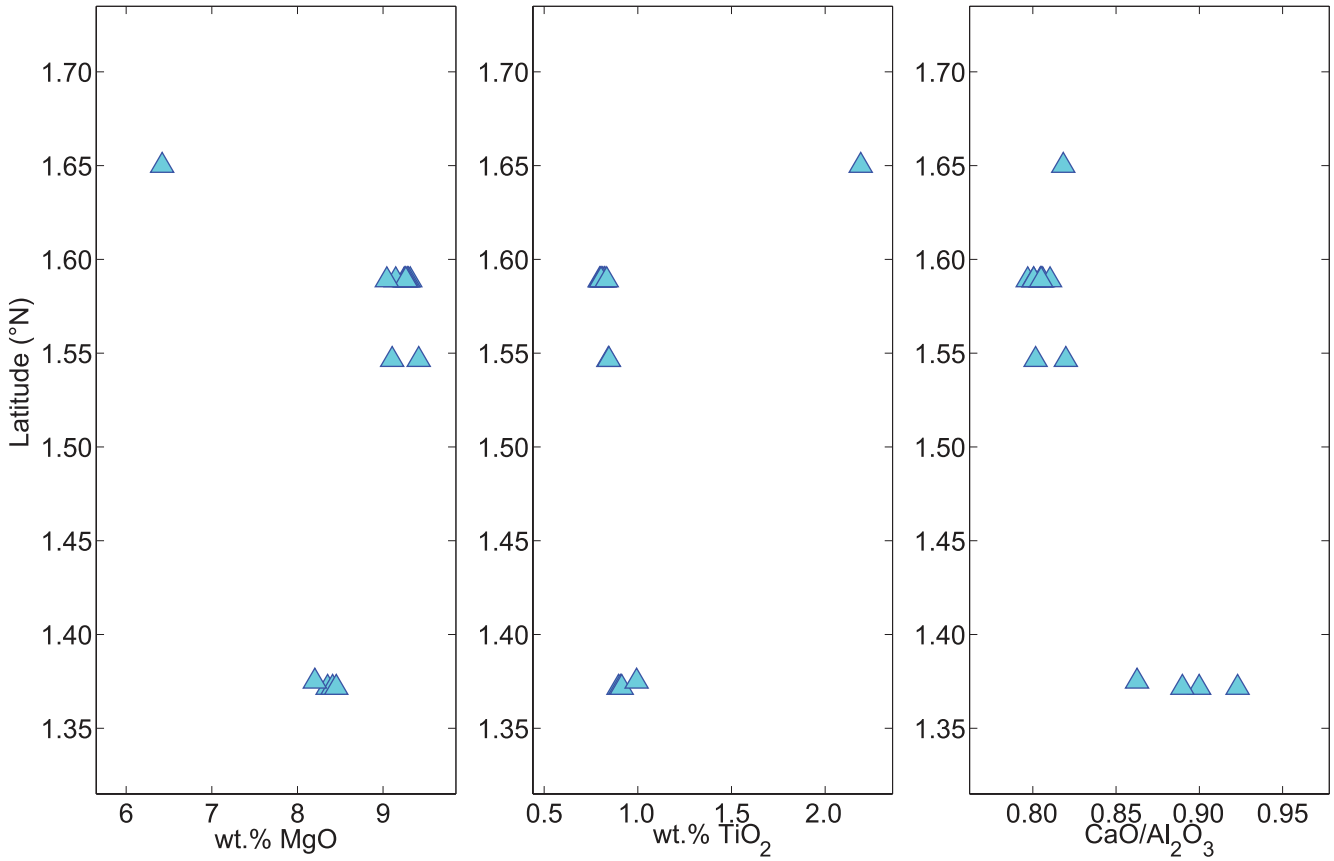

Figure 10. Calculated liquid lines of descent from the MELTS family of algorithms (Ghiorso et al., 2002). Best fit for northern GTF samples use D2-1 as a parental composition with ~0.5 wt.% H2O added, fractionating olivine and plagioclase between 1-1.5 kbar (blue circles and squares) Southern GTF lavas appear to crystallize at lower pressures (green triangles), but their relationship to a parental melt composition recovered from the GTF is inconclusive.

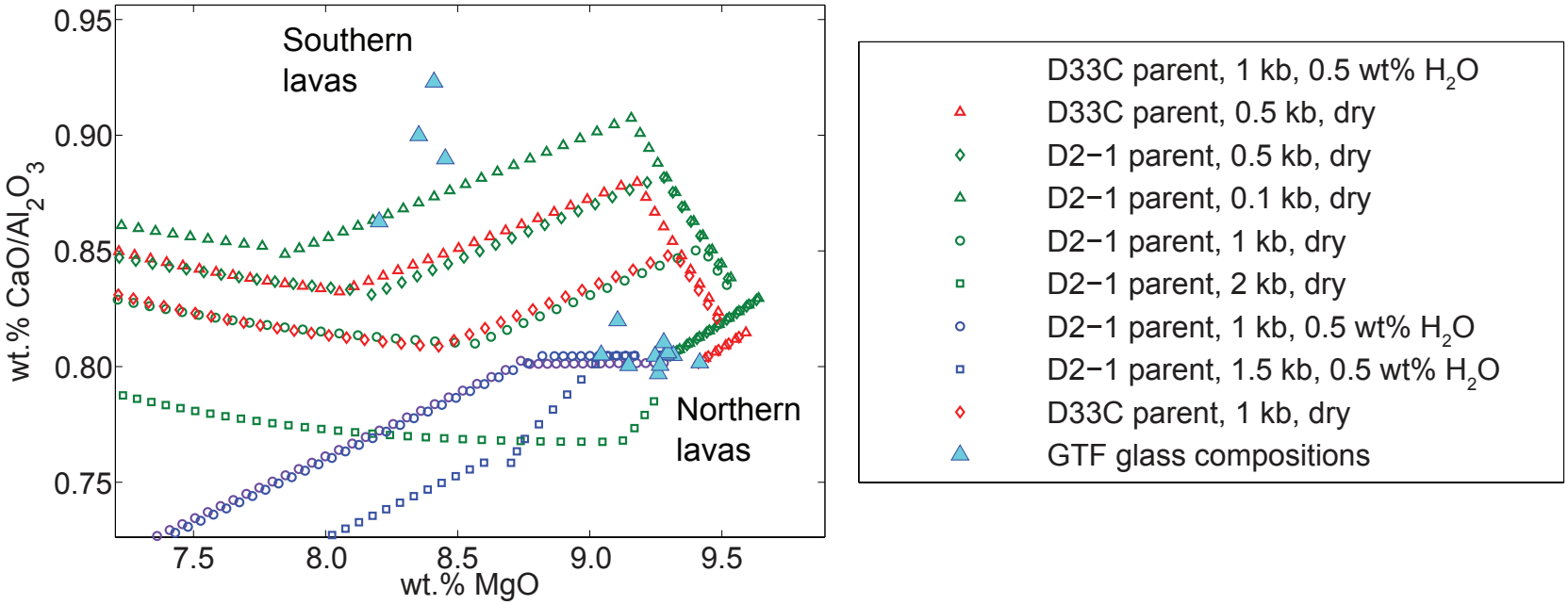

Figure 11. Electron microprobe data from GTF olivine phenocrysts. Crosses indicate core compositions, diamonds mark rim compositions. Grey field highlights the range of phenocryst compositions in chemical equilibrium with GTF glasses, assuming an olivine-glass KD of ~0.28 (Palme and O'Neill, 2008). Some olivine cores from northern samples are not in equilibrium with their host glasses.

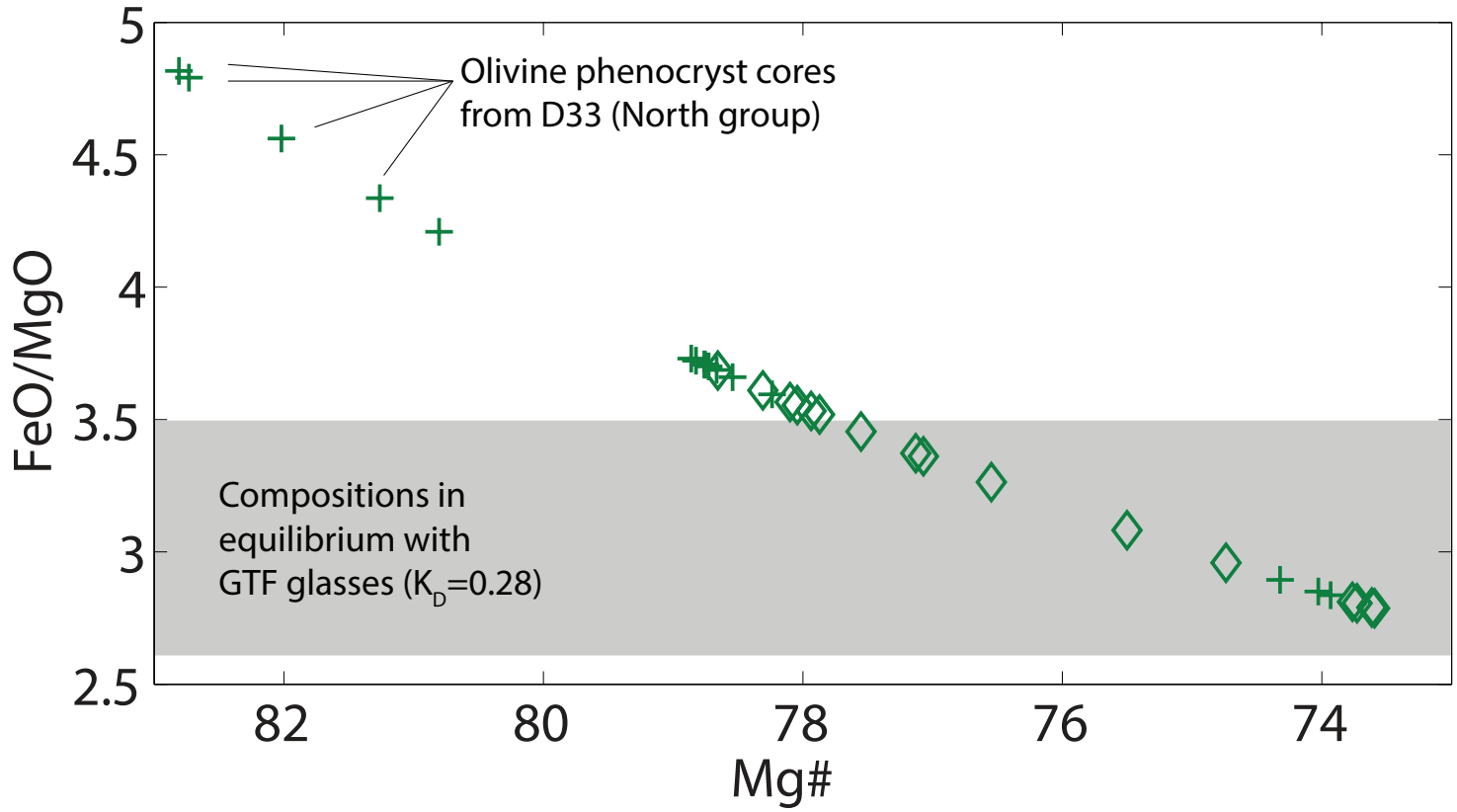

Figure 12. Rare earth element compositions of GTF samples normalized to chondrite values (McDonough and Sun 1995). A: previously published data from Cushman et al. (2004). B: previously published data from Kokfelt et al. (2005).

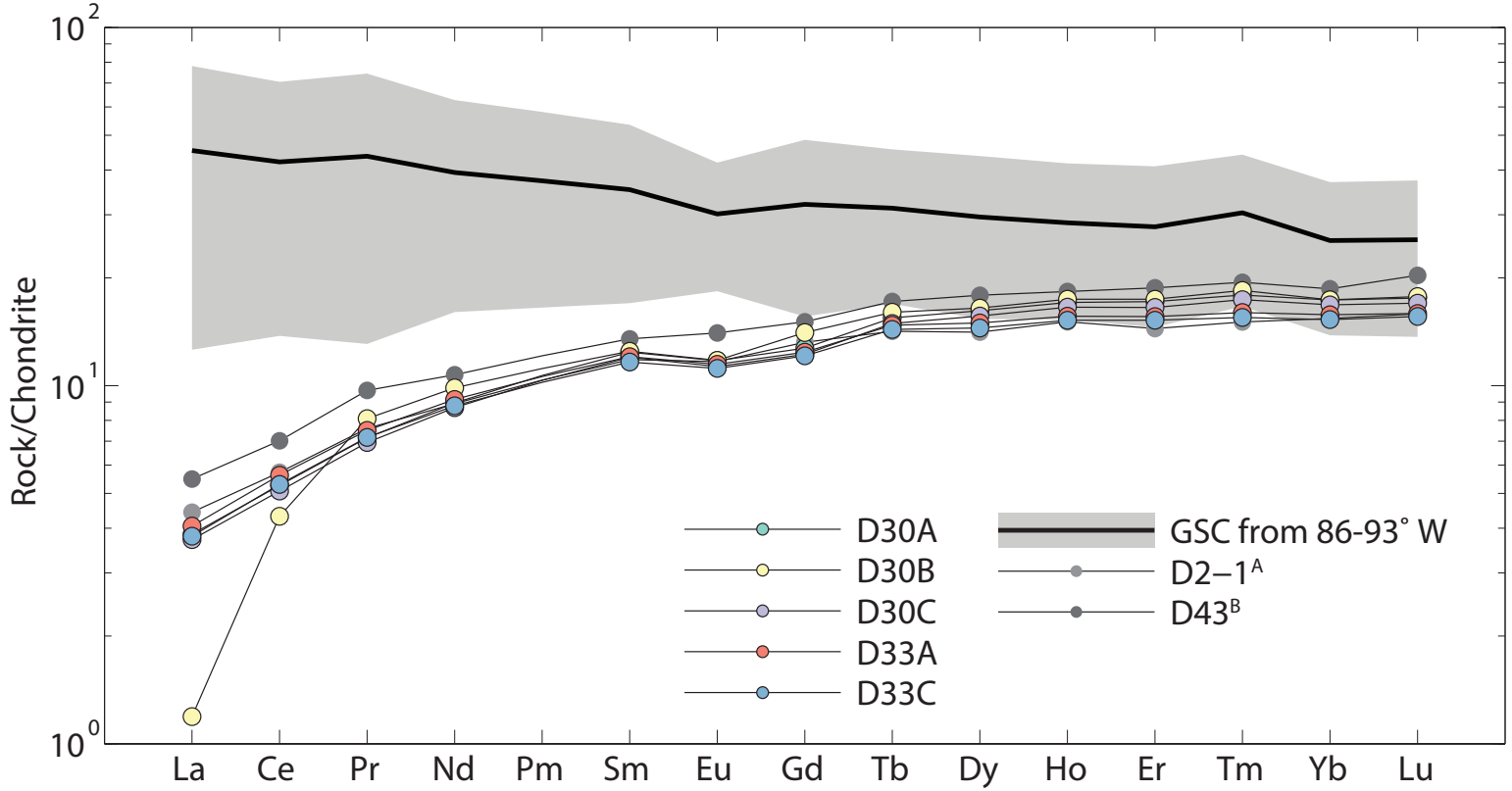

Figure 13. GTF incompatible trace element compositions, normalized to primitive mantle (McDonough and Sun, 1995). Missing data points indicate non-detectable values of Rb, Ba, and Th. See Figure 13 for previously published references for D2-1 and D43.

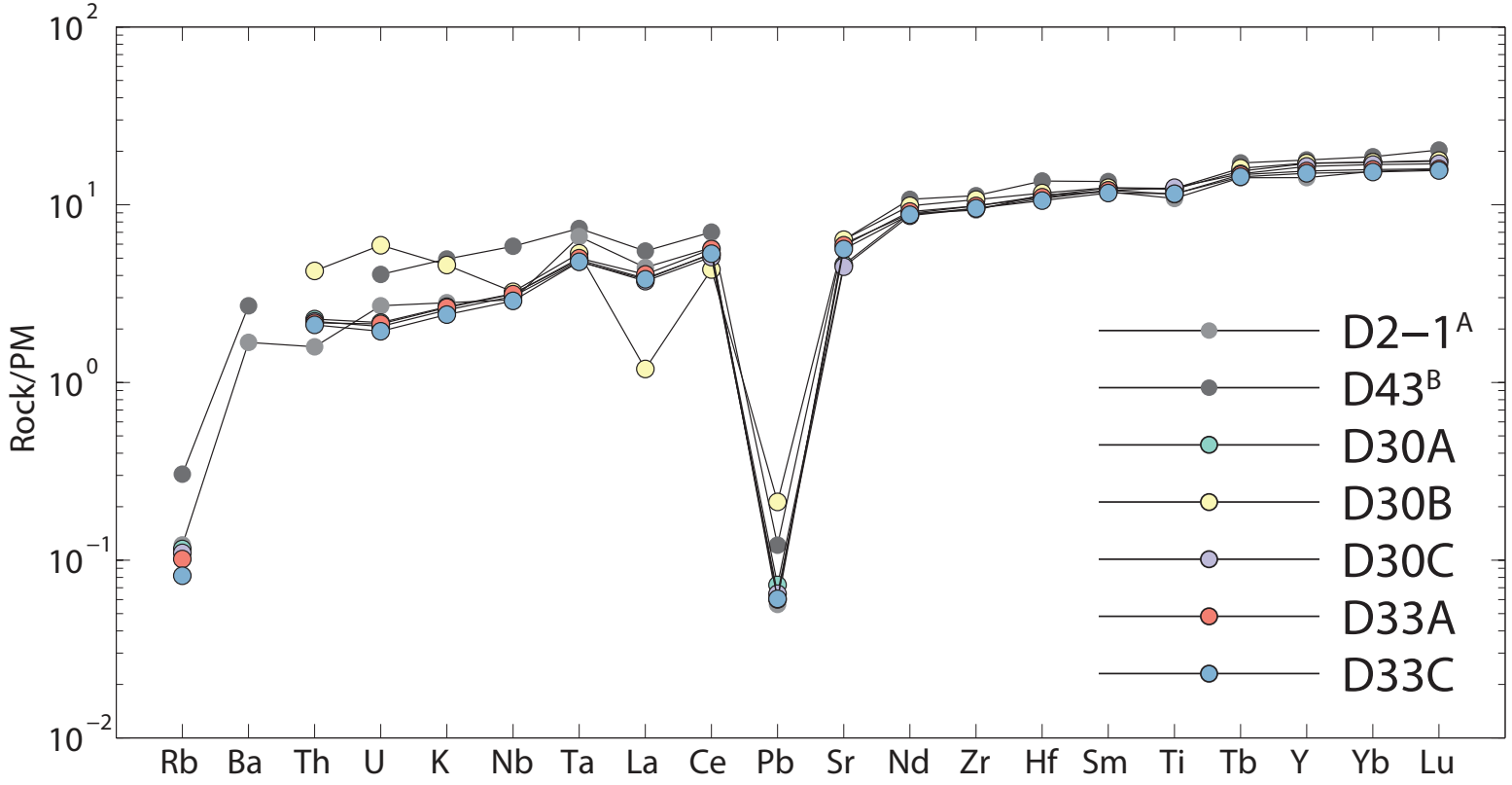

Figure 14. GTF radiogenic isotope compositions. Fields indicate range of GSC and NGVP compositions (Schillinget al., 2003; Sintonet al., 2003; Cushmanet al., 2004; Geist et al., 2005; Kokfelt et al., 2005; Ingle et al., 2010; Harpp et al., 2014a; Harpp et al., 2014b; Wilson et al., In Prep.)

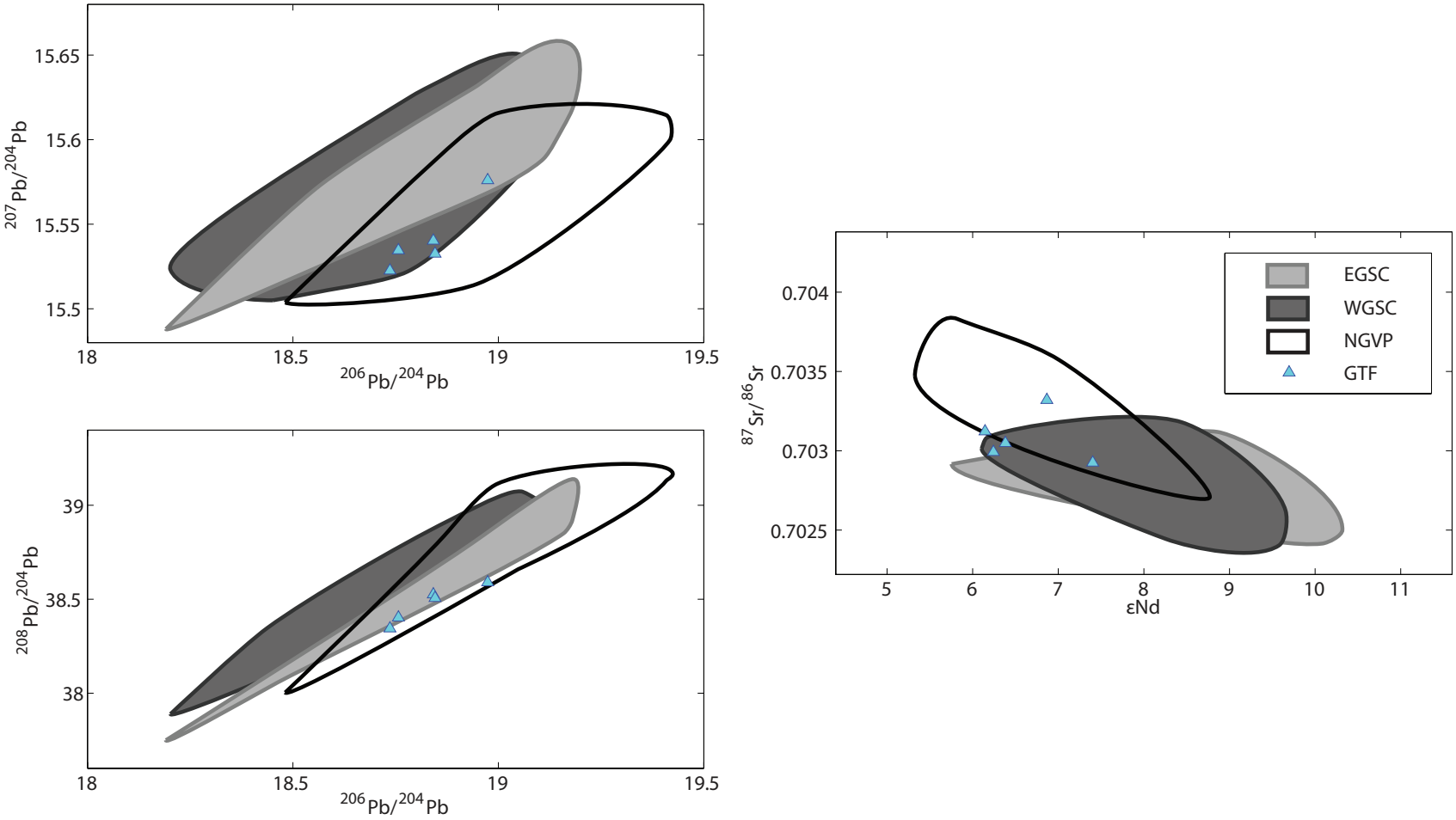

Figure 15. GTF radiogenic isotope compositions relative to latitude. Southern samples appear more depleted in radiogenic isotopes than northern samples. Symbols are larger than 2σ precision.

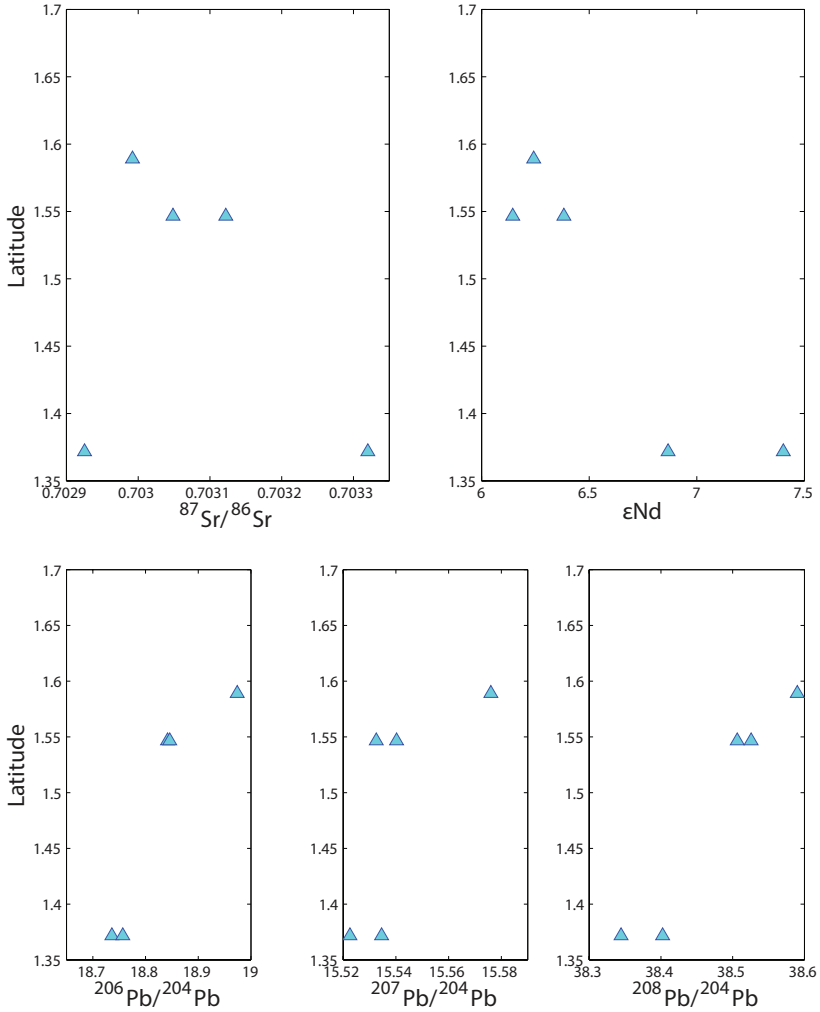

Figure 16. Compiled Galápagos Archipelago, GSC, and NGVP radiogenic isotope compositions used in PCA (Schillinget al., 2003; Sintonet al., 2003; Cushmanet al., 2004; Geist et al., 2005; Kokfelt et al., 2005; Gibsonand Geist, 2010; Ingle et al., 2010; Gibsonet al., 2012; Harpp et al., 2014a; Harpp et al., 2014b; Wilson et al., In Prep). Dark blue stars indicate PCA-derived end-members, connected with calculated mixing lines (grey). See text for further details about end-member calculations.

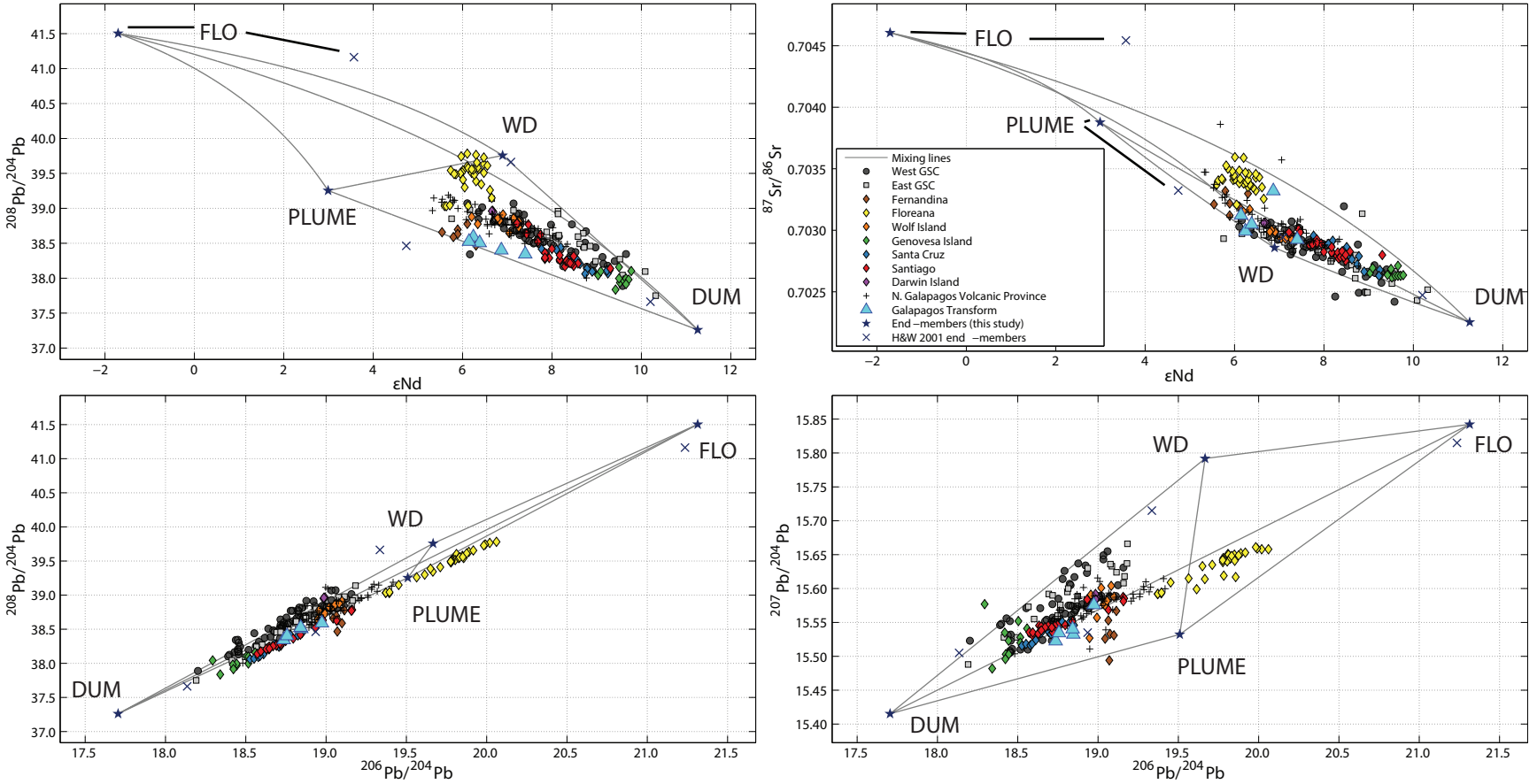

Figure 17. Principal component scores for Galápagos samples. Axes aligned with eigenvectors from PCA represent contributions from 4 mantle reservoirs: DUM, PLUME, FLO, and WD (Harpp and White, 2001). Data compiled from sources listed in Figure 16.

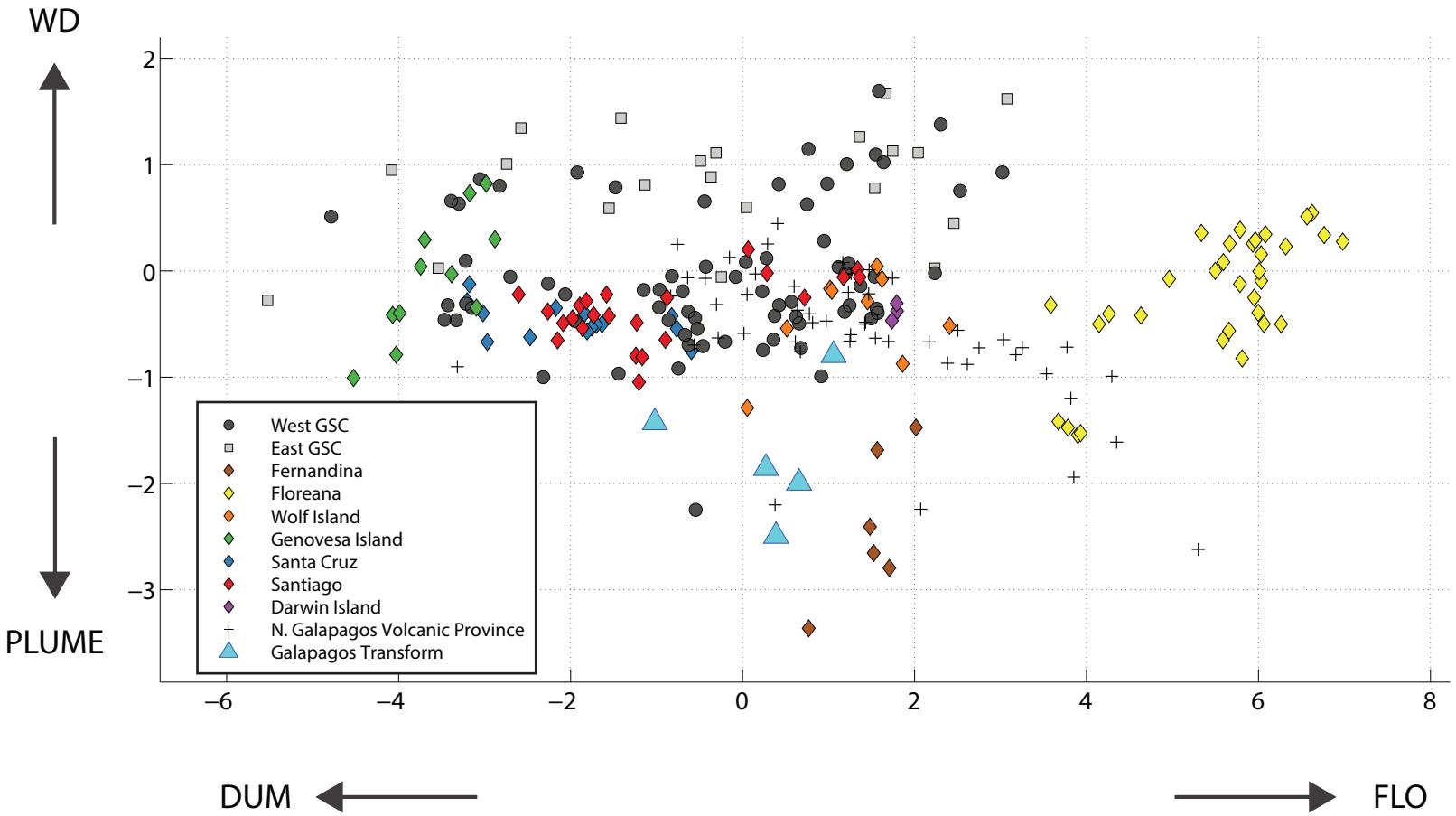

Figure 18. Density distribution plots of 10^4 admissible Metropolis-Hastings derived solutions to melt mixing model, after 10^6 iterations. Dark hexagons indicate higher probability of minimized residuals; solution density counts are listed to the right of each plot. Partial melt degrees are given on a scale of 0-1. Mixing volume fractions for melts derived from each source range from 0-1. Incompatible trace element concentrations for Sr and Nd are in parts per million (ppm). See text for further details on governing equations, model boundary conditions, and initial conditions

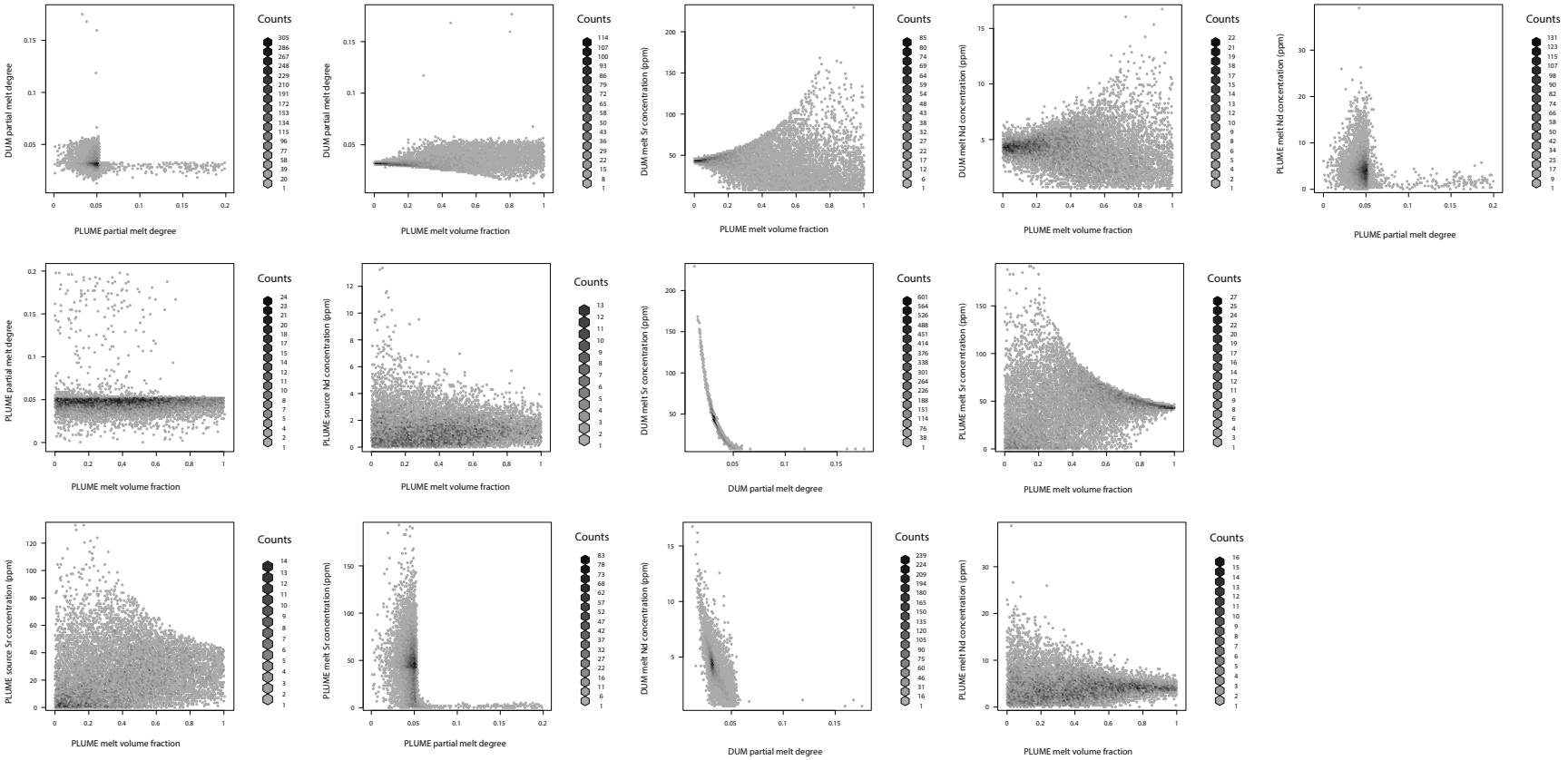

Figure 19. Boxplots of solution ranges from geologically-constrained model solutions (see text for details). Solutions reported as mean (dark bars), +/- one standard deviation (n=409, grey box), with accompanying total range of solutions (horizontal hashes) and outliers (points).

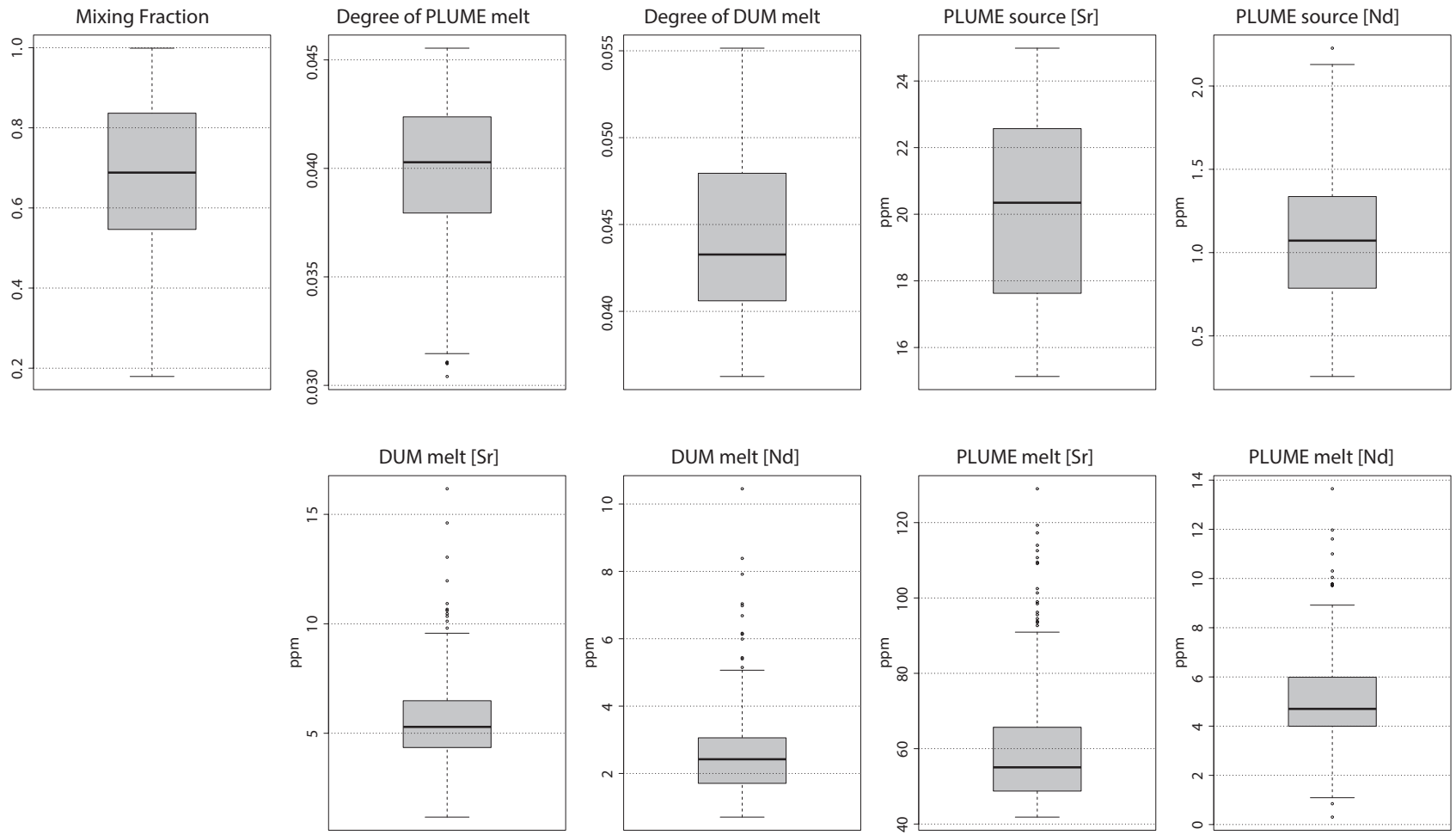

Figure 20. Bathymetric cross sections of north and south GTF. Red lines indicate bathymetry-identified fault scarps measured for horizontal offset used to estimate strain.

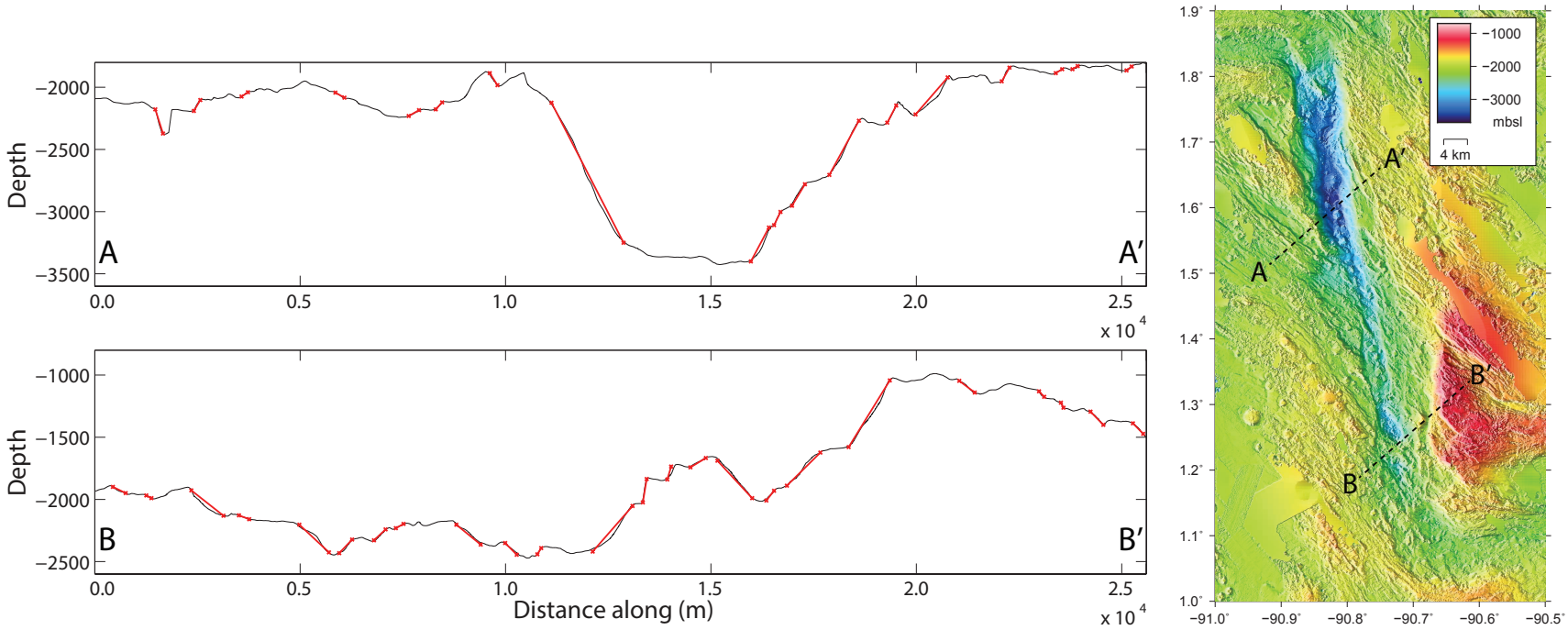

Figure 21. Pb isotope compositions for GSC, NGVP, and GTF samples plotted against longitude. GTF and some NGVP samples define the most depleted isotope compositions near the archipelago.

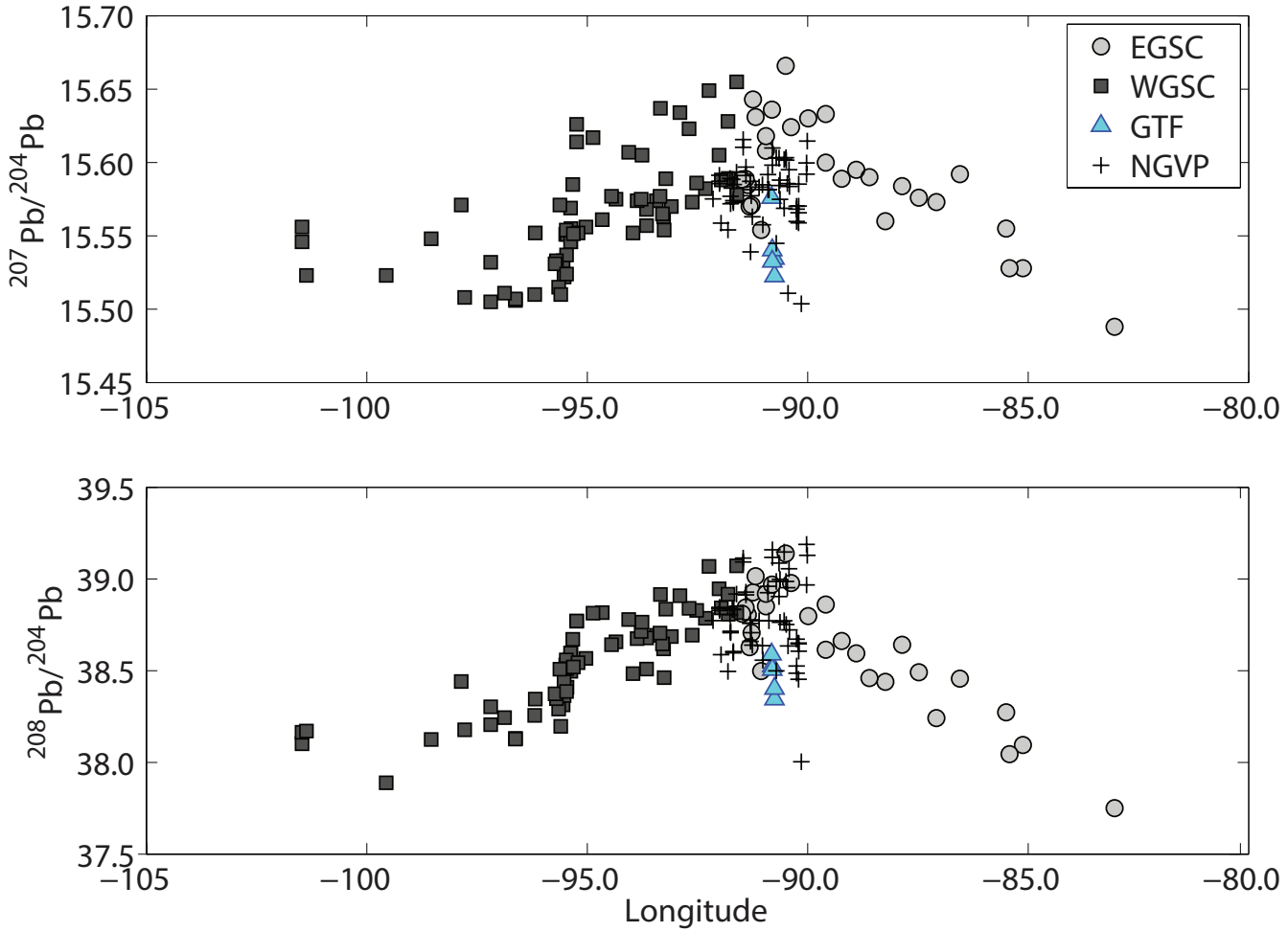

Figure 22. U/Pb and Th/Pb trace element compositions relative to $^{208}Pb/^{204}Pb$ and $^{207}Pb/^{204}Pb$ ratios for NGVP, East GSC, and West GSC samples (symbols identified in Figure 19). U/Pb and Th/Pb enrichment coupled with $^{208}Pb/^{204}Pb$ and $^{207}Pb/^{204}Pb$ enrichment, characteristic of WD-influenced lavas, suggests that the WD source is enriched in U and Th or depleted in Pb relative to PLUME and DUM components. U/Pb and Th/Pb enrichment and $^{208}Pb/^{204}Pb$ and $^{207}Pb/^{204}Pb$ enrichment can be achieved by seafloor and subduction alteration of oceanic crust (e.g., Kelley et al., 2005).

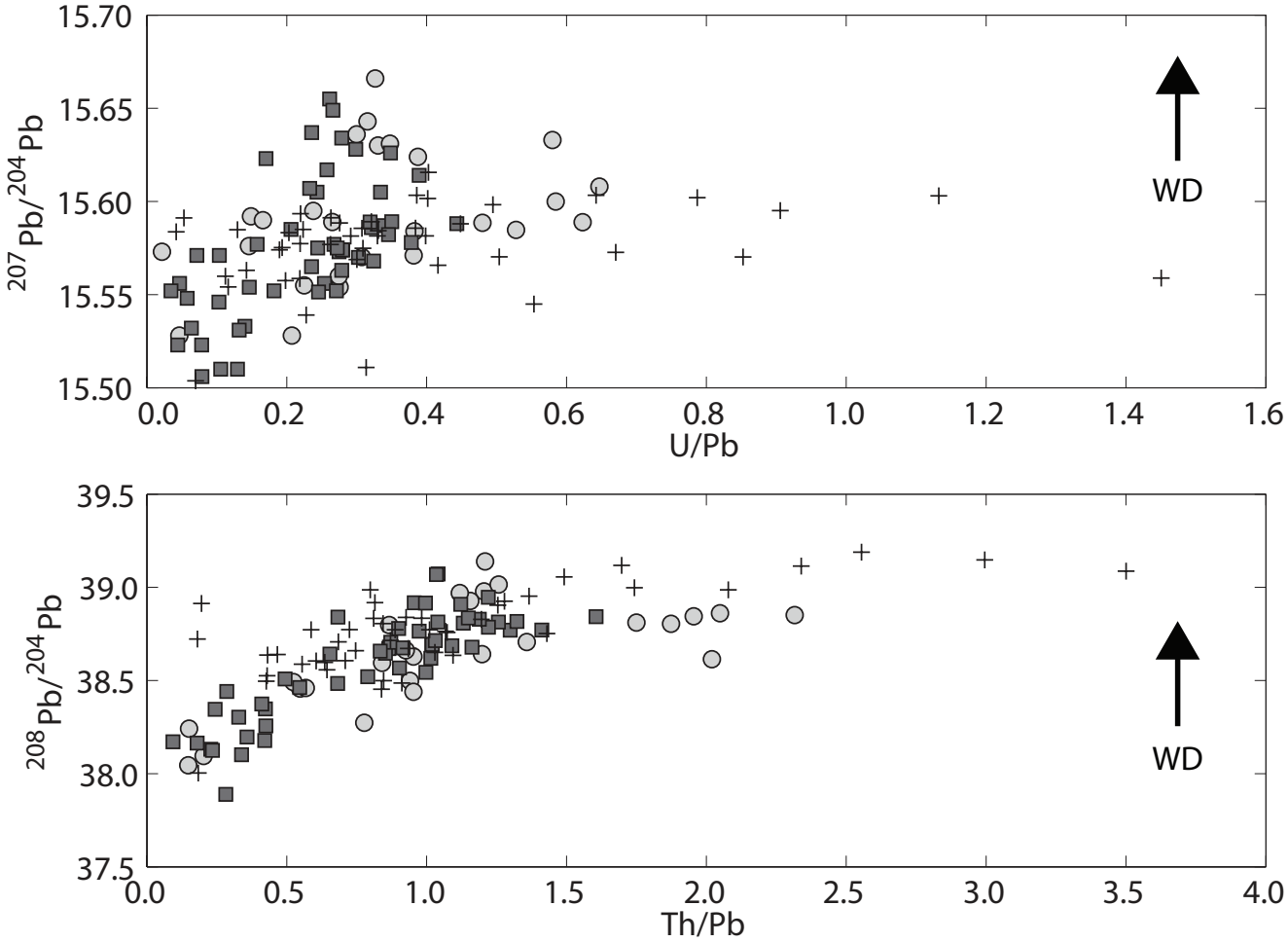

Figure 23. Enrichment in $^{208}Pb/^{204}Pb$ and, to a lesser degree, $^{207}Pb/^{204}Pb$ coupled with enrichments in light and middle rare earth elements La and Sm in the NGVP and GSC (symbols identified in Figure 19) suggest that low degree melts (elevated La/Sm and Sm/Yb) have a stronger WD signal (elevated $^{208}Pb/^{204}Pb$ and $^{207}Pb/^{204}Pb$).

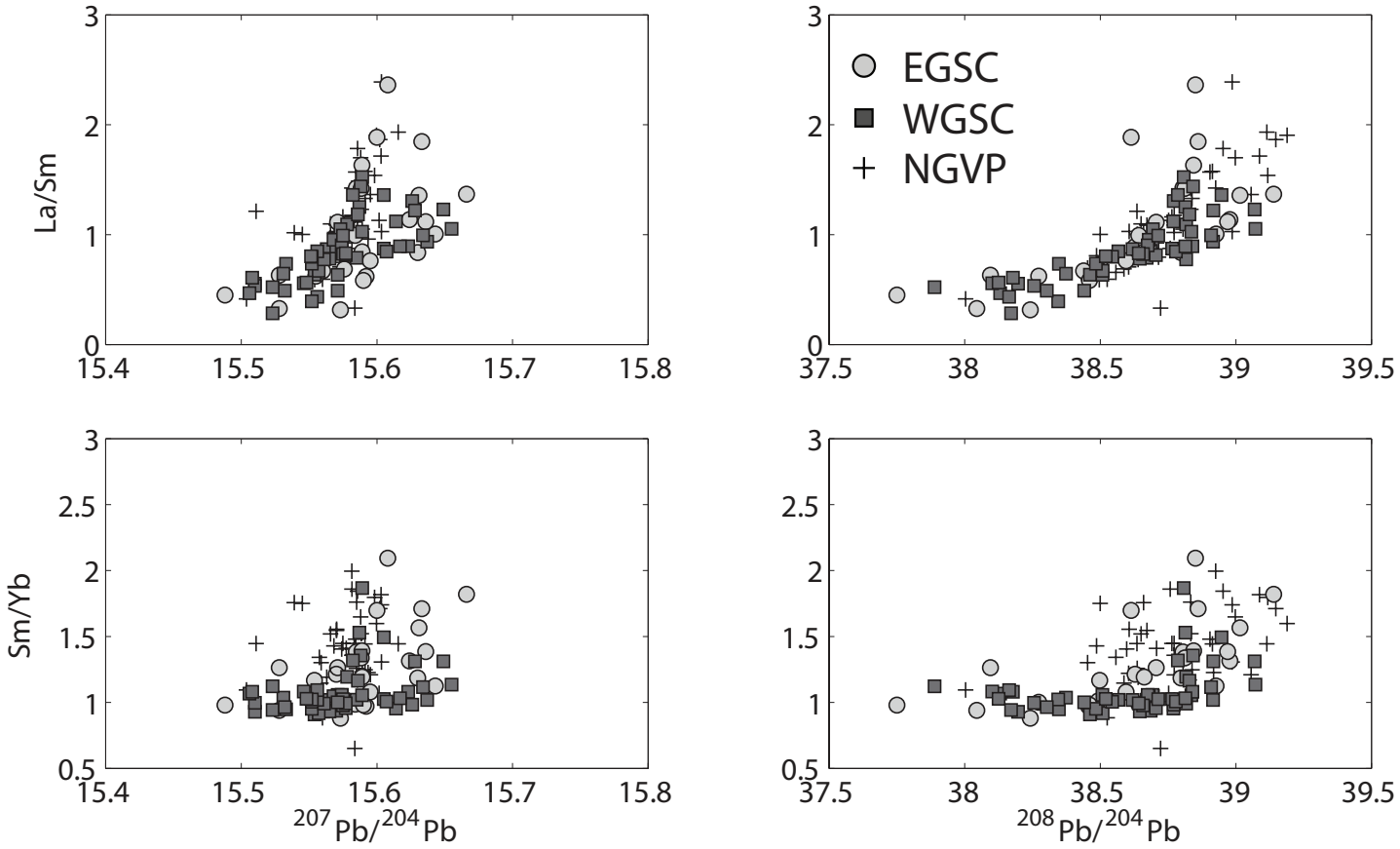

Figure 24. Mean REE composition of GSC axial lavas from 93°-89°W (gray circles), modeled GSC melt residues left from 1-10% partial melting of an enriched mantle source (Workman and Hart, 2005), and modeled mean GTF source REE compositions, using model melting constraints of 3-5% partial melting. Sources were calculated assuming pure fractional melting, using partition coefficients for spinel-stability melting depths (Workman and Hart, 2005).

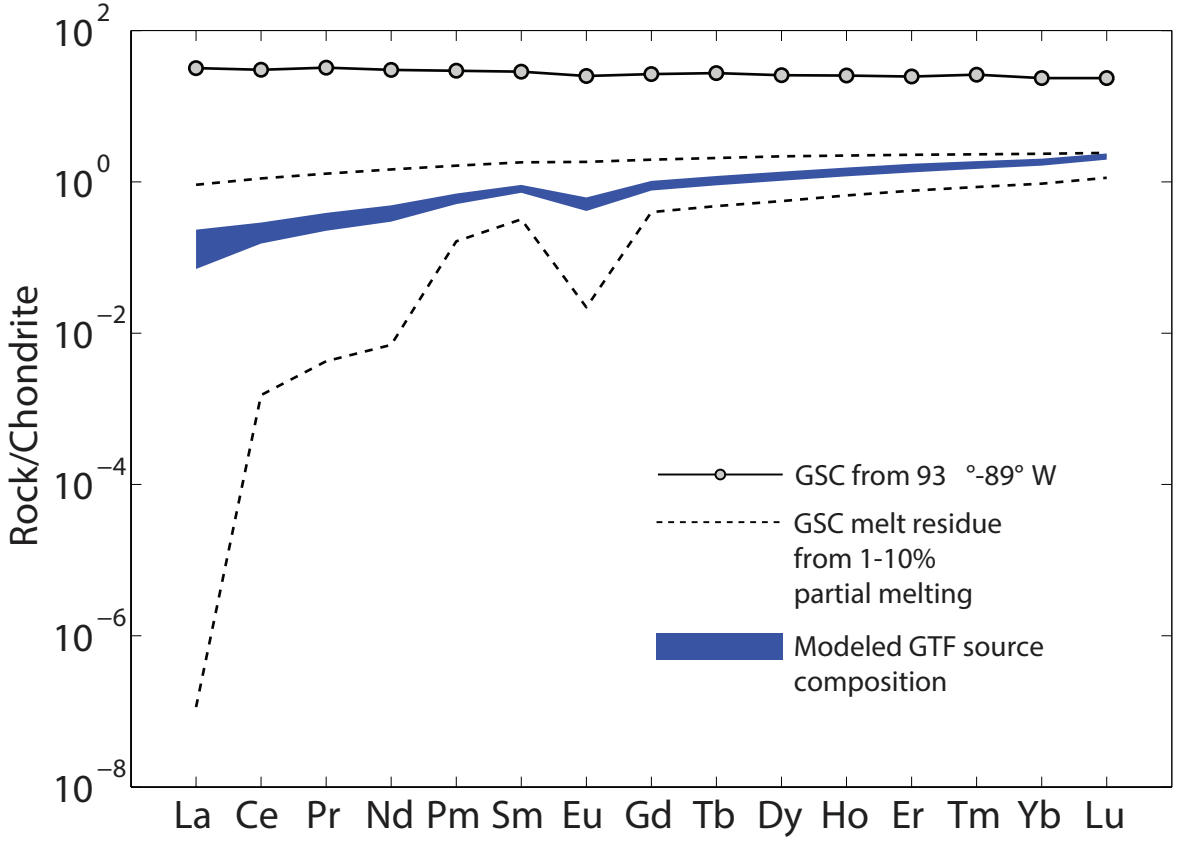

Figure 25. Illustration of extensional TF melting process, after Wendt et al. (1999). A: Extension across the TF occurs due to plate motion. B: TF develops extensional basin. C: Cross-section, illustrating melting process at extensional TFs as described by Wendt et al. (1999).